Non-Hydrostatic RegCM4 (RegCM4-NH): Model description and case studies over multiple domains.

Erika Coppola (1), Paolo Stocchi (2), Emanuela Pichelli (1), Jose Abraham Torres Alavez (1), Russel Glazer (1), Graziano Giuliani (1), Fabio Di Sante (1), Rita Nogherotto (1), Filippo Giorgi (1)

Correspondence to: Erika Coppola (coppolae@ictp.it)

1. International Centre for Theoretical Physics (ICTP),Trieste, Italy
2. Institute of Atmospheric Sciences and Climate, National Research Council of Italy, CNR-ISAC, Bologna, Italy

Abstract. We describe the development of a non-hydrostatic version of the regional climate model RegCM4, called RegCM4-NH, for use at convection-permitting resolutions. The non-hydrostatic dynamical core of the Mesoscale Model MM5 is introduced in the RegCM4, with some modifications to increase stability and applicability of the model to long-term climate simulations. Newly available explicit microphysics schemes are also described, and three case studies of intense convection events are carried out in order to illustrate the performance of the model. They are all run at convection-permitting grid spacing of 3 km over domains in northern California, Texas and the Lake Victoria region, without the use of parameterized cumulus convection. A substantial improvement is found in several aspects of the simulations compared to corresponding coarser resolution (12 km) runs completed with the hydrostatic version of the model employing parameterized convection. RegCM4-NH is currently being used in different projects for regional climate simulations at convection-permitting resolutions, and is intended to be a resource for users of the RegCM modeling system.

Keywords
Regional climate models; RegCM4; km-scale resolution; climate change

Introduction

Since the pioneering work of Dickinson et al. (1989) and Giorgi and Bates (1989), documenting the first regional climate modeling system (RegCM, version 1) in literature, the dynamical downscaling technique based on limited area Regional Climate Models (RCMs) has been widely used worldwide, and a number of RCM systems have been developed (Giorgi 2019). RegCM1 (Dickinson et al., 1989, Giorgi and Bates, 1989) was originally developed at the National Center for Atmospheric Research (NCAR) based on the Mesoscale Model version 4 (MM4) (Anthes et al, 1987) . Then, further model versions followed: RegCM2 (Giorgi et al. 1993a,b), RegCM2.5, (Giorgi and Mearns 1999), RegCM3 (Pal et al. 2007), and lastly RegCM4 (Giorgi et al 2012). Except for the transition from RegCM1 to RegCM2, in which the model dynamical core was updated from that of the MM4 to that of the MM5 (Grell et al. 1994), these model evolutions were mostly based on additions of new and more advanced physics packages. RegCM4 is today used by a large community for numerous projects and applications, from process studies to paleo and future climate projections, including participation in the Coordinated Regional Downscaling EXperiment (CORDEX, Giorgi et al. 2009; Gutowski et al. 2016). The model can also be coupled with ocean, land and chemistry/aerosol modules in a fully interactive way (Sitz et al. 2017).

The dynamical core of the standard version of RegCM4 is hydrostatic, with sigma-p vertical coordinates. As a result, the model can be effectively run for grid spacings of ~10 km or larger, for which the hydrostatic assumption is valid. However, the RCM community is rapidly moving to higher resolutions of a few km, i.e. "convection-permitting" (Prein et al. 2015; Coppola et al. 2020) and therefore the dynamical core of RegCM4 has been upgraded to include a non-hydrostatic dynamics representation usable for very high resolution applications. This upgrade, which we name RegCM4-NH, is essentially based on the implementation of the MM5 non-hydrostatic dynamical core within the RegCM4 framework, which has an entirely different set of sub-grid model physics compared to MM5.

RegCM4-NH is already being used in some international projects focusing on climate simulations at convection-permitting km-scales, namely the European Climate Prediction

59   System (EUCP, Hewitt and Lowe 2018) and the CORDEX Flagship Pilot Study dedicated

60   to convection (CORDEX-FPSCONV, Coppola et al. 2020), and it is starting to be used

61   more broadly by the RegCM modeling community.

62   For example, the recent papers by Ban et al. (2021) and Pichelli et al. (2021) document

63   results of the first multi-model experiment of 10-year simulations at the convection-

64   permitting scales over the so-called greater Alpine region. Two different simulations with

65   RegCM4-NH for present day conditions have contributed to the evaluation analysis of

66   Ban et al. (2021). They were carried out at the International Centre for Theoretical Physics

67   (ICTP) and the Croatian Meteorological and Hydrological Service (DHMZ) using two

68   different physics configurations. The results show that RegCM4-NH largely improves the

69   precipitation simulation as compared to available fine scale observations when going from

70   coarse to high resolution, in particular for higher order statistics, such as precipitation

71   extremes and hourly intensity. Pichelli et al. (2021) then analyse multi-model ensemble

72   simulations driven by selected CMIP5 GCM projections for the decades 1996–2005 and

73   2090–2099 under the RCP8.5 scenario. ICTP contributed to the experiment with

74   simulations using RegCM4-NH driven by the MOCH-HadGEM GCM (r1i1p1) in a two

75   level nest configuration (respectively at 12 and 3 km grid). The paper shows new insights

76   into future changes, for example an enhancement of summer and autumn hourly rainfall

77   intensification compared to coarser resolution model experiments, as well as an increase

78   of frequency and intensity of high-impact weather events.

79

80   In this paper we describe the structure of RegCM4-NH and provide some illustrative

81   examples of its performance, so that model users can have a basic reference providing

82   them with background information on the model. In the next section we first describe the

83   new model dynamical core, while the illustrative applications are presented in section 4.

84   Section 5 finally provides some discussion of future developments planned for the RegCM

85   system.

86

Model description

In the development of RegCM4-NH, the RegCM4 as described by Giorgi et al. (2012) was modified to include, the non-hydrostatic dynamical core (*idynamic* = 2 namelist option as described in RegCM-4.7.1/Doc/README.namelist of the source code) of the mesoscale model MM5 (Grell et al. 1994). This dynamical core was selected because RegCM4 already has the same grid and variable structure as MM5 in its hydrostatic core, which substantially facilitated its implementation (Elguindi et al. 2017).

The model equations with complete description of the Coriolis force and a top radiative boundary condition, along with the finite differencing scheme, are given in Grell et al. (1994). Pressure, p, temperature, T, and density, ϱ, are first decomposed into a prescribed reference vertical profile plus a time varying perturbation. The prognostic equations are then calculated using the pressure perturbation values. Compared to the original MM5 dynamical core, the following modifications were implemented in order to achieve increased stability for long term climate simulations (Elguindi et al. 2017 document any modifications which follow the choice of the non-hydrostatic dynamical core through the namelist parameter *idynamic* = 2; further available user-dependant options, and the corresponding section in the namelist, are explicitly indicated):

i) The reference state temperature profile is computed using a latitude dependent climatological temperature distribution and thus is a function of the specific domain coordinates (*base_state_pressure*, *logp_lrate* parameters in *&referenceatm*) (Elguindi et al. 2017). These two parameters were hard-coded in the original MM5 while for the RegCM are user configurable;

ii) The lateral time dependent boundary conditions (*iboudy* in *&physicsparam*) for each prognostic variable use the same exponential relaxation technique (*iboudy* = 5) described in Giorgi et al. (1993). The linear MM5 relaxation scheme is also kept as an option (*iboudy* = 1);

117   iii) The advection term in the model equations, which in the MM5 code is implemented

118   using a centered finite difference approach, was changed to include a greater upstream

119   weight factor as a function of the local Courant number (Elguindi et al. 2017). The

120   maximum value of the weight factor is user configurable (*uoffc* in *&dynparam*). As detailed

121   in the MM5 model description (Grell et al., 1994), the horizontal advection term for a scalar

122   variable X contributes to the total tendency as:

123

$$\Delta_{adv}\left(p^*X\right)_G = -m^2|_G\left[\frac{\left(p^*X|_b\frac{u}{m}|_b - p^*X|_a\frac{u}{m}|_a\right)}{dx} + \frac{\left(p^*X|_d\frac{v}{m}|_d - p^*X|_c\frac{v}{m}|_c\right)}{dy}\right]$$

124

125

126   where the m is the projection mapping factor and, with respect to Figure 1, assuming that

127   the computation is to be performed for the gold cross point G, the averages are performed

128   in the points a, b, c, d. For the u/m and v/m terms, the average value is computed using

129   respectively the values in points AC, BD, CD, AB.

130   In RegCM4 for the term p^*X, the model computes a weighted average value of the field

131   using the value in gold+cyan and gold+green cross points with weights increasing the

132   relative contribution of the upstream point up as a function of the local courant number:

133

134    $p^*X|_a = 0.5((1 - f_1)p^*X|_G + (1 + f_1)p^*X|_{c_1})$

135    $p^*X|_b = 0.5((1 - f_1)p^*X|_{c_2} + (1 + f_1)p^*X|_G)$

136    $p^*X|_c = 0.5((1 - f_2)p^*X|_G + (1 + f_2)p^*X|_{g_1})$

137    $p^*X|_d = 0.5((1 - f_2)p^*X|_{g_2} + (1 + f_2)p^*X|_G)$

138   where f_1, f_2 are defined as the local Courant number for the 1D advection equations

139   multiplied for a control factor:

140

141    $f_1 = \mu_{fc}dt\frac{(u|_a + u|_b)}{2dx}$

142    $f_2 = \mu_{fc}dt\frac{(v|_c + v|_d)}{2dy}$;

143

144
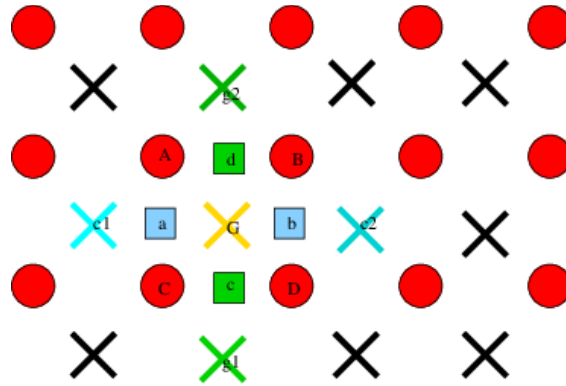
Figure 1 Schematic representation showing the horizontal advection scheme staggering. Circles are U,V points. X are scalar variable points.

iv) The water species (cloud, ice,rain, snow) term uses the same advection scheme as the other variables (Elguindi et al. 2017) and not a complete upstream scheme as in the MM5 code (Grell et al. 1994);

v) A local flux limiter reduces the advection terms in order to remove unrealistic strong gradients and its limits are user configurable (in the *&dynparam* section the maximum gradient fraction for advection: temperature, *t_extrema*, specific humidity, *q_rel_extrema*, liquid cloud content, *c_rel_extrema* and for tracers, *t_rel_extrema*). This was hardcoded in the MM5 code and the limits were not user configurable;

vi) The diffusion stencil of the Laplace equation uses a nine point approach as in LeVeque (2006) and a topography dependent environmental diffusion coefficient is added to reduce spurious diffusion along pressure coordinate slopes (Elguindi et al. 2017) as in the hydrostatic version of the code (Giorgi et al. 1993b). The change in stencil does not affect the overall fourth order precision of the model, but reduces the computational stencil size, thus reducing the communication overhead;

vii) The top boundary radiative condition (*ifupr* = 1 in *&nonhydroparam*) adopted in the semi-implicit vertical differencing scheme to reduce the reflection of energy waves uses coefficients on a 13x13 matrix which are re-computed every simulation day and not kept

170 constant throughout the whole simulation as in the MM5 code. This allows the model to

171 be run for longer simulation times while not being strongly tied to the initial atmospheric

172 conditions;

173

174 viii) The dynamical control parameter β in the semi-implicit vertical differencing scheme

175 (*nhbet* in *&nonhydroparam*) used for acoustic wave damping (Elguindi et al. 2017) is user

176 configurable (Klemp and Dudhia, 2008), while it is hard-coded in the MM5;

177

178 ix) A Rayleigh damping (*ifrayd* = 1 in *&nonhydroparam*) of the status variables towards

179 the input GCM boundary conditions can be activated in the top layers (*rayndamp*

180 configuring the number of top levels to apply) with a configurable relaxation time

181 (*rayalpha0*, Klemp and Lilly, 1978, Durran and Klemp, 1983. This is consistent to what is

182 implemented in the WRF model);

183

184 x) The water species time filtering uses the Williams (2009) modified filter with α = 0.53

185 instead of the RA filter used by all the other variables. The ν factor in the RA filter is user

186 configurable (*gnu1* and *gnu2* in *&dynparam*). This reduces the damping introduced by the

187 Robert-Asselin filter and the computational diffusion introduced by the horizontal

188 advection scheme.

189

190 With these modifications, the model basic equations, under leap-frog integration scheme,

191 are (Elguindi et al. 2017) :

192

193

$$\frac{\partial p^* u}{\partial t} = -m^2 \left[\frac{\partial p^* uu/m}{\partial x} + \frac{\partial p^* vu/m}{\partial y} \right] - \frac{\partial p^* u\dot{\sigma}}{\partial \sigma} + uDIV -$$

$$\frac{mp^*}{\rho} \left[\frac{\partial p'}{\partial x} - \frac{\sigma}{p^*} \frac{\partial p^*}{\partial x} \frac{\partial p'}{\partial \sigma} \right] + p^* fv - p^* ew \cos\theta + D_u \quad (1)$$

194

195

$$\frac{\partial p^* v}{\partial t} = -m^2 \left[\frac{\partial p^* uv/m}{\partial x} + \frac{\partial p^* vv/m}{\partial y} \right] - \frac{\partial p^* v\dot\sigma}{\partial \sigma} + vDIV -$$

$$\frac{mp^*}{\rho} \left[\frac{\partial p'}{\partial y} - \frac{\sigma}{p^*} \frac{\partial p^*}{\partial y} \frac{\partial p'}{\partial \sigma} \right] - p^* fu + p^* ew \sin\theta + D_v \qquad (2)$$

$$\frac{\partial p^* w}{\partial t} = -m^2 \left[\frac{\partial p^* uw/m}{\partial x} + \frac{\partial p^* vw/m}{\partial y} \right] - \frac{\partial p^* w\dot\sigma}{\partial \sigma} + wDIV +$$

$$p^* g \frac{\rho_0}{\rho} \left[\frac{1}{p^*} \frac{\partial p'}{\partial \sigma} + \frac{T_v'}{T} - \frac{T_0 p'}{T p_0} \right] - p^* g \left[(q_c + q_r) \right] + p^* e \left(u \cos\theta - v \sin\theta \right) + D_w \quad (3)$$

$$\frac{\partial p^* p'}{\partial t} = -m^2 \left[\frac{\partial p^* up'/m}{\partial x} + \frac{\partial p^* vp'/m}{\partial y} \right] - \frac{\partial p^* p'\dot\sigma}{\partial \sigma} + p'DIV -$$

$$m^2 p^* \gamma p \left[\frac{\partial u/m}{\partial x} - \frac{\sigma}{mp^*} \frac{\partial p^*}{\partial x} \frac{\partial u}{\partial \sigma} + \frac{\partial v/m}{\partial y} - \frac{\sigma}{mp^*} \frac{\partial p^*}{\partial y} \frac{\partial v}{\partial \sigma} \right] + \rho_0 g \gamma p \frac{\partial w}{\partial \sigma} + p^* \rho_0 g \quad (4)$$

$$\frac{\partial p^* T}{\partial t} = -m^2 \left[\frac{\partial p^* uT/m}{\partial x} + \frac{\partial p^* vT/m}{\partial y} \right] - \frac{\partial p^* T\dot\sigma}{\partial \sigma} + TDIV +$$

$$\frac{1}{\rho c_p} \left[p^* \frac{Dp'}{Dt} - \rho_0 g p^* w - D_{p'} \right] + p^* \frac{\dot Q}{c_p} + D_T \qquad (5)$$

Where:

$$DIV = m^2 \left[\frac{\partial p^* u/m}{\partial x} + \frac{\partial p^* v/m}{\partial y} \right] + \frac{\partial p^* \dot\sigma}{\partial \sigma}$$

$$\dot\sigma = -\frac{\rho_0 g}{p^*} w - \frac{m\sigma}{p^*} \frac{\partial p^*}{\partial x} u - \frac{m\sigma}{p^*} \frac{\partial p^*}{\partial y} v$$

$$\tan\theta = -\cos\phi \frac{\partial\lambda/\partial y}{\partial\phi/\partial x}$$

$$p(x,y,z,t) = p_0(z) + p'(x,y,z,t)$$
$$T(x,y,z,t) = T_0(z) + T'(x,y,z,t)$$
$$\rho(x,y,z,t) = \rho_0(z) + \rho'(x,y,z,t)$$

with the vertical sigma coordinate defined as:

$$\sigma = \frac{(p_0 - p_t)}{(p_s - p_t)}$$

212

213

214 p_s is the surface pressure and p_0 is the reference pressure profile. The total pressure

215 at each grid point is thus given as:

216

217 $$p(x, y, z, t) = p^* \sigma(k) + p_t + p'(x, y, z, t)$$

218

219 With p_t being the top model pressure assuming a fixed rigid lid.

220 The model physics schemes for boundary layer, radiative transfer, land and ocean

221 surface processes, cloud and precipitation processes are extensively described in Giorgi

222 et al. (2012) and summarized in Table 1. For each physics component a number of

223 parameterization options are available (Table 1), and can be selected using a switch

224 selected by the user. As mentioned, the use of non-hydrostatic dynamics is especially

225 important when going to convection-permitting resolutions of a few km (Prein et al. 2015).

226 At these resolutions the scale separation assumption underlying the use of cumulus

227 convection schemes is not valid any more, and explicit cloud microphysics

228 representations are necessary. The RegCM4 currently includes two newly implemented

229 microphysics schemes, the Nogherotto-Tompkins (Nogherotto et al. 2016) and the WSM5

230 scheme from the Weather Research Forecast (WRF, Skamarok et al. 2008) model, which

231 are briefly described in the next sections for information to model users.

232

Model physics (*Namelist flag*)	Options	*n. option*	Reference
Dynamical core (*idynamic*)	Hydrostatic	1	Giorgi et al. 1993a,b Giorgi et al. 2012
	Non-Hydrostatic (*)	2	present paper
Radiation	CCSM	0	Kiehl et al. 1996

(*irrtm*)	RRTM (*)	1	Mlawer et al. 1997
Microphysics (*ipptls*)	Subex	1	Pal et al 2000
	Nogherotto Thompkins	2	Nogherotto et al. 2016
	WSM5 (*)	3	Hong et al 2004
Cumulus (*icup*)	Kuo	1	Anthes et al. 1987
	Grell	2	Grell 1993
	Emanuel	4	Emanuel 1991
	Tiedtke	5	Tiedtke 1989, 1993
	Kain-Fritsch	6	Kain and Fritsch, 1990; Kain 2004
	MM5 Shallow cumulus (only mixing) (*)	-1	Grell et al. 1994
Planetary Boundary Layer (*ibltyp*)	Modified-Holtslag	1	Holtslag et al., 1990
	UW	2	Bretherton et al. 2004
Land Surface (*code compiling option*)	BATS	/	Dickinson et al. 1993; Giorgi et al. 2003
	CLM4.5	/	Oleson et al. 2013
Ocean Fluxes (*iocnflx*)	BATS	1	Dickinson et al. 1993
	Zeng	2	Zeng et al. 1998

	COARE	3	Fairall et al. 1996a,b
Interactive lake (*lakemod*)	1D diffusion/convection	1	Hostetler et al. 1993
Tropical band (*i_band*)	RegT-Band	1	Coppola et al. 2012
Coupled ocean (*iocncpl*)	RegCM-ES	1	Sitz et al. 2017

Table 1 Core and sub-grid physics scheme available in RegCM-NH. New schemes available with this release are starred (*).

Explicit microphysics schemes

Nogherotto-Tompkins Scheme

A new parameterization for explicit cloud microphysics and precipitation built upon the European Centre for Medium Weather Forecast's Integrated Forecast System (IFS) module (Tiedtke [1993], Tompkins [2007]), was introduced in RegCM4 (*ipptls* = 2 in *µparam*) by Nogherotto et al. [2016]. In the present configuration, the scheme implicitly solves 5 prognostic equations for water vapor, qv, cloud liquid water, ql, rain, qr, cloud ice, qi, and snow, qs, but it is also easily extendable to a larger number of variables. Water vapor, cloud liquid water, rain, cloud ice and snow are all expressed in terms of the grid-mean mixing ratio.

Cloud liquid and ice water content are independent, allowing the existence of supercooled liquid water and mixed-phase clouds. Rain and snow precipitate with a fixed terminal fall speed and can then be advected by the three dimensional winds. A check for the conservation of enthalpy and of total moisture is ensured at the end of each timestep. The governing equation for each variable is:

$$\frac{\partial q_x}{\partial t} = S_x + \frac{1}{\rho}\frac{\partial}{\partial z}(\rho V_x q_x)$$

253

254

255   The local variation of the mixing ratio qx of the variable x is given by the sum of

256 Sx, containing the net sources and sinks of qx through microphysical processes (i.e.

257 condensation, evaporation, auto-conversion, melting, etc.), and the sedimentation term,

258 which is a function of the fall speed Vx . An upstream approach is employed to solve the

259 equations. The sources and sinks contributors are divided in two groups according to the

260 duration of the process they describe: processes that are considered to be fast relative to

261 the model time step are treated implicitly while slow processes are treated explicitly. The

262 processes taken into account (shown in Figure 2) are the microphysical pathways across

263 the 5 water variables: condensation, autoconversion, evaporation, cloud water collection

264 (accretion), and autoconversion for warm clouds, and freezing, melting, deposition,

265 sublimation for cold clouds.

266
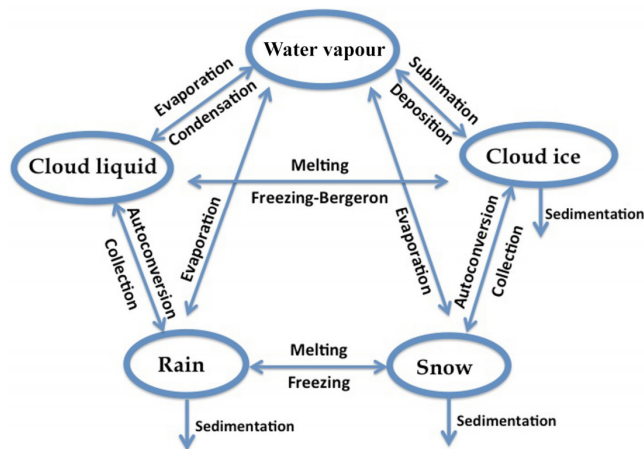
267

268 **Figure 2: Depiction of the new scheme, showing the five prognostic variables and**

269 **how they are related to each other through microphysical processes**

270 For each microphysical pathway, phase changes are associated with the release or

271 absorption of latent heat, which then impacts the temperature budget. The impact is

272 calculated using the conservation of liquid water temperature TL defined as:

273

$$T_L = T - \frac{L_v}{C_p}(q_l + q_r) - \frac{L_s}{C_p}(q_i + q_s).$$

274

275 Given that dTL =0, the rate of change of the temperature is given by the following
276 equation:

277

$$\frac{\partial T}{\partial t} = \sum_{x=1}^{m} \frac{L(x)}{C_p} \left(\frac{dq_x}{dt} - D_{q_x} - \frac{1}{\rho}\frac{\partial}{\partial z}(\rho V_x q_x) \right)$$

278
279

280 where $L(x)$ is the latent heat of fusion or evaporation, depending on the process
281 considered, Dqx is the convective detrainment and the third term in brackets is the
282 sedimentation term.

283 At the end of each time step a check is carried out of the conservation of total water and

284 moist static energy: $h = C_P T + gz + Lq_x.$

285 The scheme is tunable through parameters in the *µparam* section of the namelist
286 (RegCM-4.7.1/Doc/README.namelist; Elguindi et al. 2017).

287

288 **WSM5 Scheme**

289 RegCM4-NH also employs the Single-Moment 5-class microphysics scheme of the WRF
290 model (Skamarock et al., 2008). This scheme (ipptls = 3 in µparam) follows Hong
291 et al. (2004) and, similarly to Nogherotto et al. (2016), includes vapor, rain, snow, cloud
292 ice, and cloud water hydrometeors. The scheme separately treats ice and water
293 saturation processes, assuming water hydrometeors for temperatures above freezing,
294 and cloud ice and snow below the freezing level (Dudhia, 1989, Hong et al., 1998). It
295 accounts for supercooled water and a gradual melting of snow below the melting layer
296 (Hong et al., 2004, and Hong and Lim, 2006). Therefore, the WSM5 and Nogherotto-
297 Tompkins schemes have similar structures (Figure 2), but also important differences.

298 Differently from the Nogherotto-Tompkins scheme, the WSM5 (as well as the other WSM
299 schemes in WRF) prescribes an inverse exponential continuous distribution of particle
300 size (ex. Marshall and Palmer (1948) for rain, Gunn and Marshall (1958) for snow). It also
301 includes the size distribution of ice particles and, as a major novelty, the definition of the
302 number of ice crystals based on ice mass content rather than temperature. Both the
303 Nogherotto-Tompkins and WSM5 schemes include autoconversion, i.e. sub-time step
304 processes of conversion of cloud water to rain and cloud ice to snow. For rain, Hong et
305 al. (2004) use a Kessler (1969) type algorithm in WSM5, but with a stronger physical basis
306 following Tripoli and Cotton (1980). The Nogherotto-Tompkins scheme also includes the
307 original Kessler (1969) formula as an option, but it makes available other three
308 exponential approaches following Sundqvist et al. (1989), Beheng (1994), and
309 Khairoutdinov and Kogan (2000). For ice autoconversion the Nogherotto-Tompkins
310 scheme uses an exponential approach (Sundqvist, 1989) with a specific coefficient for ice
311 particles (following Lin et al., 1983) depending on temperature, while the WSM5 uses a
312 critical value of ice mixing ratio (depending on air density) and a maximum allowed ice
313 crystal mass (following Rutledge and Hobbs, 1983) that suppresses the process at low
314 temperatures because of the effect of air density. Finally, the WSM5 has no dependency
315 on cloud cover for condensation processes while the Nogherotto-Tompkins scheme uses
316 cloud cover to regulate the condensation rate in the formation of stratiform clouds.

317 *Illustrative case studies*

318

319   Three case studies (Table 2) of Heavy Precipitation Events (HPE) have been identified in

320   order to test and illustrate the behavior of the non-hydrostatic core of the RegCM4-NH,

321   with focus on the explicit simulation of convection over different regions of the world. In

322   two of the test cases, California and Lake Victoria, data from the ERA-Interim reanalysis

323   (Dee et al. 2011) are used to provide initial and lateral meteorological boundary conditions

324   (every 6 hours) for an intermediate resolution run (grid spacing of 12 km, with use of

325   convection parameterizations), which then provides driving boundary conditions for the

326   convection-permitting experiments (Figure 3). In the Texas case study, however, we

327   nested the model directly in the ERA-Interim reanalysis given that such configuration

328   was able to accurately reproduce the HPE intensity. In this case the model uses a large

329   LBC relaxation zone which allows the description of realistic fine-scale features driving

330   this weather event (although not fully consistent with the Matte et al. (2017) criteria). All

331   simulations start 24-48 hours before the HPE (Table 2). The analysis focuses on the total

332   accumulated precipitation over the entire model domain at 3 km resolution (Figure 2) for

333   the periods defined in Table 2. In the cases of California and Texas the evaluation also

334   includes the time series of 6 hourly accumulated precipitation averaged on the region of

335   maximum precipitation (black rectangles in Figures 5a and 7a) because high temporal

336   resolution observations (NCEP/CPC) are also available (Table 3). The discussion of the

337   case studies is presented in the next sections; the configuration files (namelists) with full

338   settings for the three test cases are available at https://zenodo.org/record/5106399.

339

340   A key issue concerning the use of CP-RCMs is the availability of very high resolution,

341   high quality observed datasets for the assessment and evaluation of the models, which

342   is lacking for most of the world regions. Precipitation measurements come from

343   essentially three distinct sources: in-situ rain-gauges, ground radar and satellite. In the

344   present study we use 7 observational datasets depending on the case study and the area

345   covered, as described in Table 3. We have used: Precipitation Estimation from Remotely

346   Sensed Information using Artificial Neural Networks - Climate Data Record (PERSIAN-

347   CDR), Climate Hazards Group InfraRed Precipitation with Station data (CHIRPS), the

348   Climate Prediction Center morphing method (CMORPH), Tropical Rainfall Measuring

349   Mission (TRMM), NCEP/CPC-Four Kilometer Precipitation Set Gauge and Radar

350 (NCEP/CPC), CPC-Unified gauge-based daily precipitation estimates (CPC) and

351 Parameter-elevation Regressions on Independent Slopes Model (PRISM) (Table 3).

352 NCEP/CPC is a precipitation analysis which merges a rain gauge dataset with radar

353 estimates. CMORPH and PERSIAN-CDR are based on satellite measurements, CHIRPS

354 incorporates satellite imagery with in-situ station data. CPC is a gauge-based analysis of

355 daily precipitation. The PRISM dataset gathers climate observations from a wide range

356 of monitoring networks, applying sophisticated quality control measures and developing

357 spatial climate datasets which incorporate a variety of modeling techniques at multiple

358 spatial and temporal resolutions.

359

Case	ACRONYM	Region of The event	Domains size lon x lat x vertical levels	Simulation Time Window (UTC)
1	CAL	California	480 x 440 x 41	15 Feb 2004 00:00 19 Feb 2004 00:00
2	TEX	Texas	480 x 440 x 41	9 June 2010 00:00 12 June 2010 00:00
3	LKV	Lake Victoria	550 x 530 x 41	25 Nov 1999 00:00 1 Dec 1999 00:00

360 **Table 2: List of acronyms and description of the test cases with corresponding**

361 **3km domain sizes and simulation period.**

362

Dataset name	Region	Spatial Resolution	Temporal Resolution	Data Source	Reference
TRMM	World	0.5°	Daily	Satellite	Huffman et al. (2007)

CHIRPS	World	0.05°	Daily	Station data+Satellite	Funk et al. (2015)
CMORPH	World	0.25°	Daily	Satellite	Joyce et al. (2004)
NCEP/CPC	USA	0.04°	Hourly	*Gauge and Radar*	https://doi.org/10.5065/D69Z93M3. Accessed: 27/06/2018
CPC	World	0.5°	Daily	Station data	Chen and Xie (2008)
PRISM	USA	0.04°	Daily	Station data	PRISM Climate Group. 2016.
PERSIAN-CDR	World	0.25°	Daily	Satellite	Ashouri et al. (2015)

363 **Table 3: List of observed precipitation datasets used for comparison.**

364

365
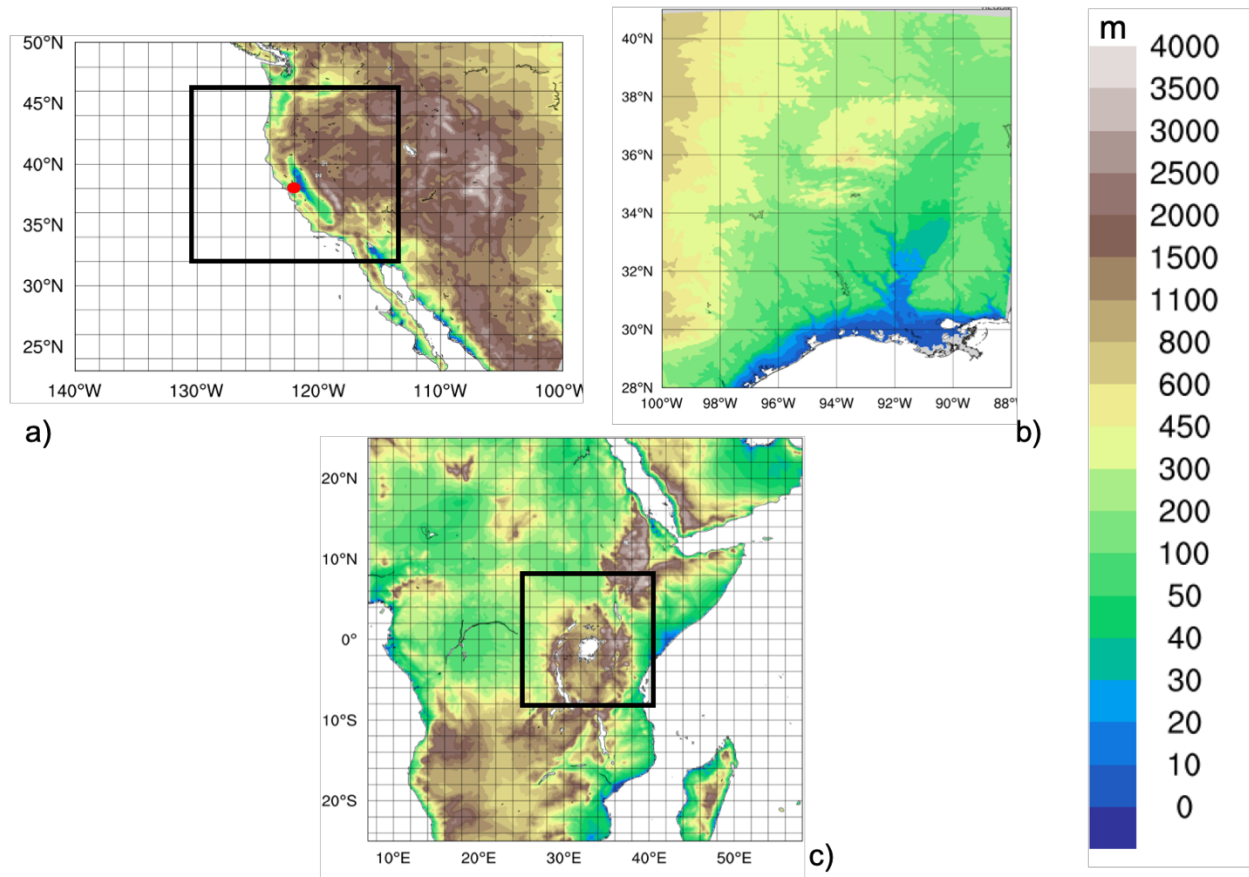
Figure 3: Domains tested , a) California (CAL) , b) Texas (TEX), c) Lake Victoria (LKV) . For CAL (a) and LKV (b) the black square shows the 3 km simulation domains nested in the 12 km domain in figure. For TEX case (b) the 3 km domain simulation is fed directly with the ERA-Interim reanalysis fields.

370

371

California

The first case, referred to as CAL in Table 2, is a HPE which occurred on February 16-18 2004, producing flooding conditions for the Russian River, a southward-flowing river in the Sonoma and Mendocino counties of northern California (red-dot in Figure 3a). The event is documented in detail by Ralph et al. (2006), who focused their attention on the impact of narrow filament-shaped structures of strong horizontal water vapor transport

378   over the eastern Pacific Ocean and the western U.S. coast, called Atmospheric Rivers

379   (ARs). ARs are typically associated with a low-level jet stream ahead of the cold front of

380   extratropical cyclones (Zhu and Newell 1998; Dacre et al. 2015; Ralph et al. 2018), and

381   can induce heavy precipitation where they make landfall and are forced to rise over

382   mountain chains (Gimeno et al. 2014). The CAL event consists of a slow propagating

383   surface front arching southeastward towards Oregon and then southwestward offshore

384   of California (Figure 4a,c). Rain began over the coastal mountains of the Russian River

385   watershed at 0700 UTC of February 16, as a warm front descended southward, and also

386   coincided with the development of orographically favoured low-level upslope flow (Ralph

387   et al., 2006).
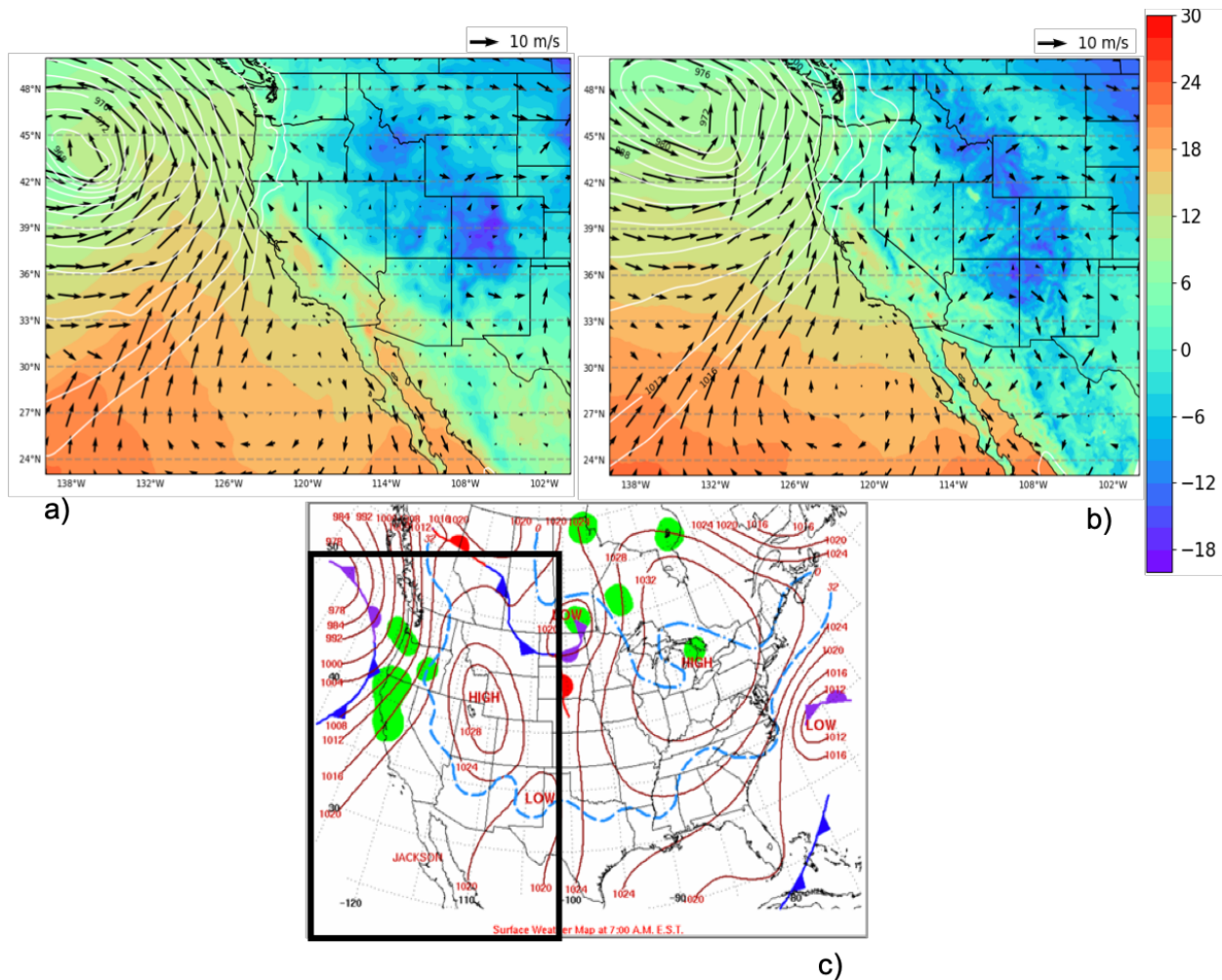
388

389   **Figure 4: a,b) mean sea level pressure (mslp, hPa, white contour lines), surface**

390   **temperature (color shading, °C) and 100-m wind direction (black arrows, m/s) at 0700 UTC,**

February 16, 2004 of ERA5 reanalysis and RegCM 12km respectively. c) NCEP-NOA Surface Analysis of pressure and fronts. The black box in (c) bounded the area represented in (a) and (b)

The intermediate resolution (12 km) domain (Figure 3a) covers a wide area encompassing California and a large portion of the coastal Pacific Ocean, with 23 vertical levels and a parameterization for deep convection based on the Kain–Fritsch scheme (Kain, 2004). The ERA-Interim driven simulation is initialized at 0000 UTC, February 15 2004 (Table 2) and lasts until 0000 UTC February 19 2004. This simulation is used as a boundary conditions for a RegCM4-NH run over a smaller area centered over northern California (Fig. 3a) at 3 km horizontal resolution, with 41 vertical levels and boundary conditions updated every 6 hours. In RegCM4-NH only the shallow convection code of the Tiedtke scheme (Tiedtke, 1996) is activated. Simulated precipitation is compared with the CHIRPS, CMORPH, TRMM, PRISM, NCEP/CPC observations (Table 3).

As shown in Figure 4 the February 16 synoptic conditions for mean sea level pressure (mslp), surface temperature and wind direction of this case study, are well reproduced by RegCM4 at 12 km (Fig. 4b) when compared to ERA5 reanalysis (Fig. 4a). The surface analysis of pressure and fronts derived from the operational weather maps prepared at the National Centers for Environmental Prediction, Hydrometeorological Prediction Center, National Weather Service (https://www.wpc.ncep.noaa.gov/dailywxmap/index_20040216.html) is also reported in Figure 4c.

The available observed precipitation datasets show similar patterns for the total accumulated precipitation (Figure 5), in particular CHIRPS (Figure 5a), PRISM (Figure 5d) and NCEP (Figure 5e) exhibit similar spatial details and magnitudes of extremes. CHIRPS shows a maximum around 42°N which is not found in the other datasets. CMORPH (Figure 5b) and TRMM (Figure 5c) show lower precipitation maxima and lesser spatial details due to their lower resolution, indicating that the performance of satellite-based products may be insufficient as a stand alone product to validate the model for this case.

420 The largest observed maxima are placed on the terrain peaks, with extreme rainfall
421 greater than 250 mm in 60 hours over the coastal mountains and between 100 – 175 mm
422 elsewhere (Fig. 5). The black box in Fig 5a shows the area of the Russian River
423 watershed where the largest rainfall rates were detected (269 mm and 124 mm in 60-h
424 accumulated rainfall between 0000 UTC February 16 and 1200 UTC February 18, 2004,
425 respectively) (Ralph et al., 2006).

426 The convection-permitting simulation captures the basic features of the observed
427 precipitation, both in terms of spatial distribution (Fig. 5f) and of temporal evolution of
428 rainfall (Fig. 6a). However, it shows higher precipitation rates than observed over the sea
429 and over the mountain chains, with lower intensities than observed in the south-east part
430 of the mountain chain (Fig. 5). The 12-km simulation instead severely underestimates the
431 magnitude of the event (Fig. 5g).

432 Figure 6a shows the 6-hourly accumulated precipitation averaged over the black box in
433 Figure 5a. The 3 km and 12 km simulations capture the onset of the event, but the peak
434 intensity is strongly underestimated by the 12 km run, while it is well simulated by the 3
435 km run, although the secondary maximum is overestimated. These results demonstrate
436 that only the high resolution convection-permitting model is able to captures this extreme
437 event, and that parameterized convection has severe limits in this regard (Done et al.
438 2004; Lean et al. 2008; Weisman et al. 2008; Weusthoff et al. 2010; Schwartz 2014; Clark
439 et al. 2016).

440
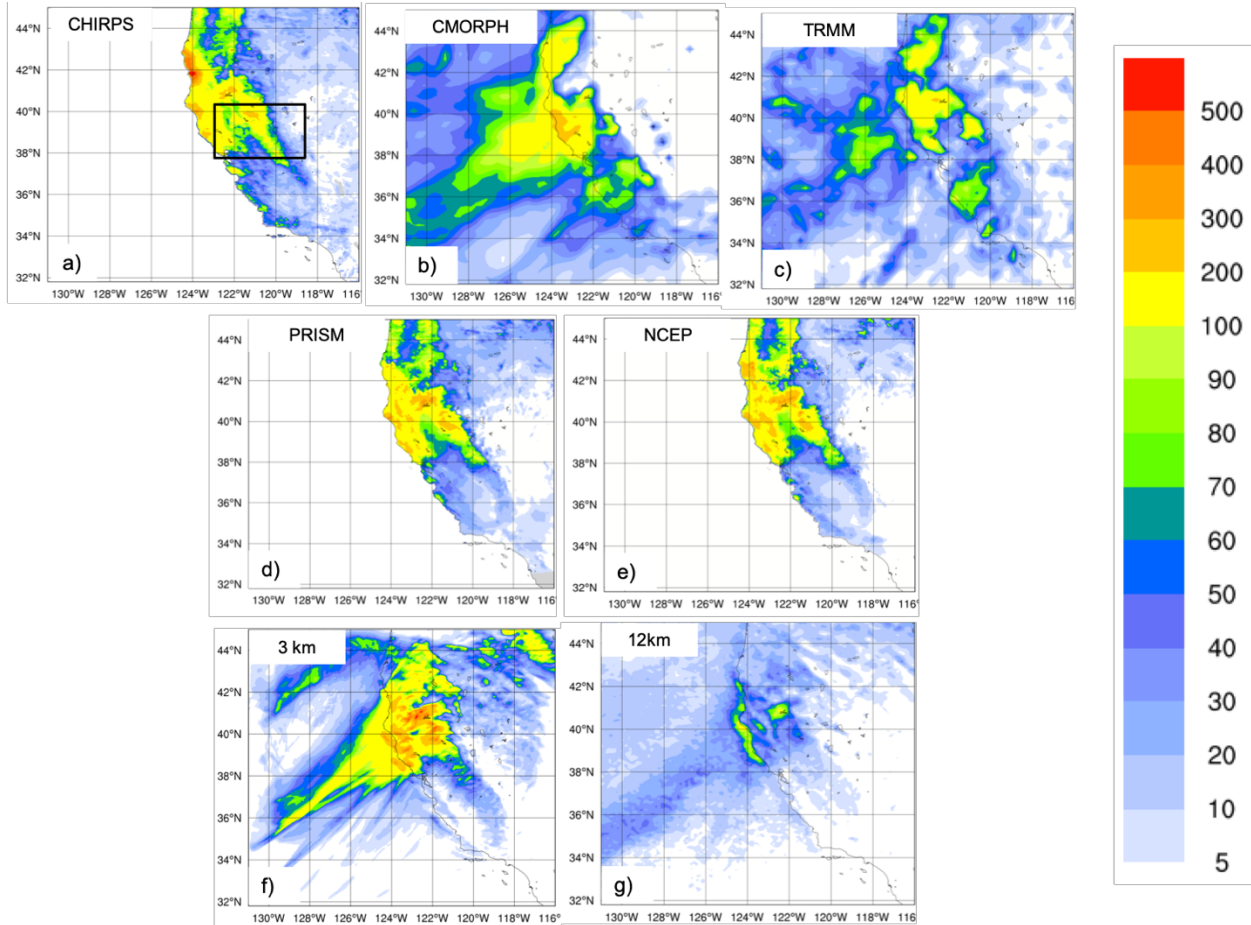
Figure 5 : Total accumulated precipitation (mm) during the California case: CHIRPS (a), CMORPH (b), TRMM (c) observations, PRISM (d) and NCEP Reanalysis (e) and convection-permitting simulation with RegCM4-NH at 3km (f) and RegCM4 at 12km (g). The black box denotes the area where the spatial average of 6-hourly accumulated precipitation is calculated for Figure 6a.

446

447

448

449

450

CAL (a)   TEX (b)
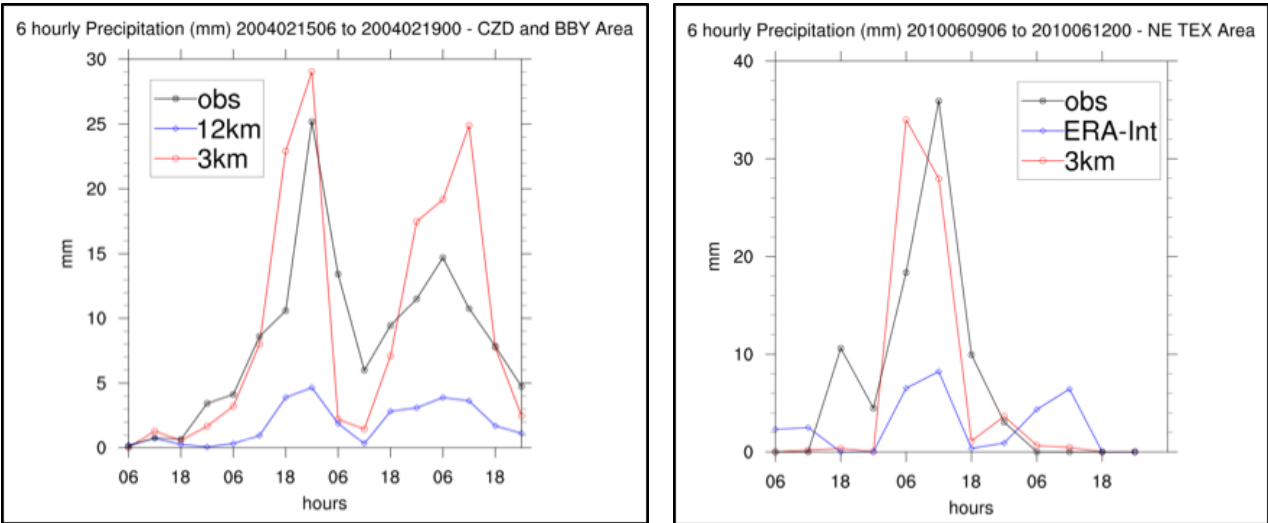
Figure 6: Time series of the 6 hourly accumulated precipitation (in mm on the y-axis) during the CAL event (a) and during the TEX event (b). The blue lines show RegCM4 12 Km and ERA interim 6 hourly accumulated precipitation averaged over the areas indicated by the black squares in Figures 5 and 7 while the red line shows the 6 hourly accumulated precipitation simulated by RegCM4-NH. The observations are shown with a black line.

Texas

Case 2, hereafter referred to as TEX (Table 2), is a convective precipitation episode exhibiting characteristics of the "Maya Express" flood events, linking tropical moisture plumes from the Caribbean and Gulf of Mexico to midlatitude flooding over the central United States (Higgins 2011). During the TEX event, an upper-level cutoff low over northeastern Texas, embedded within a synoptic-scale ridge, moved slowly northeastward. Strong low-level flow and moisture transport from the western Gulf of Mexico progressed northward across eastern Texas. The event was characterized by low-level moisture convergence, weak upper-level flow, weak vertical wind shear, and relatively cold air (center of cutoff low), which favored the slow-moving convective storms and nearly stationary thunderstorm outflow boundaries. The main flooding event in

468 eastern Texas occurred on June 10, 2010, with a daily maximum rainfall of 216.4 mm for

469 the region in the black box of Figure 7a (Higgins 2011).
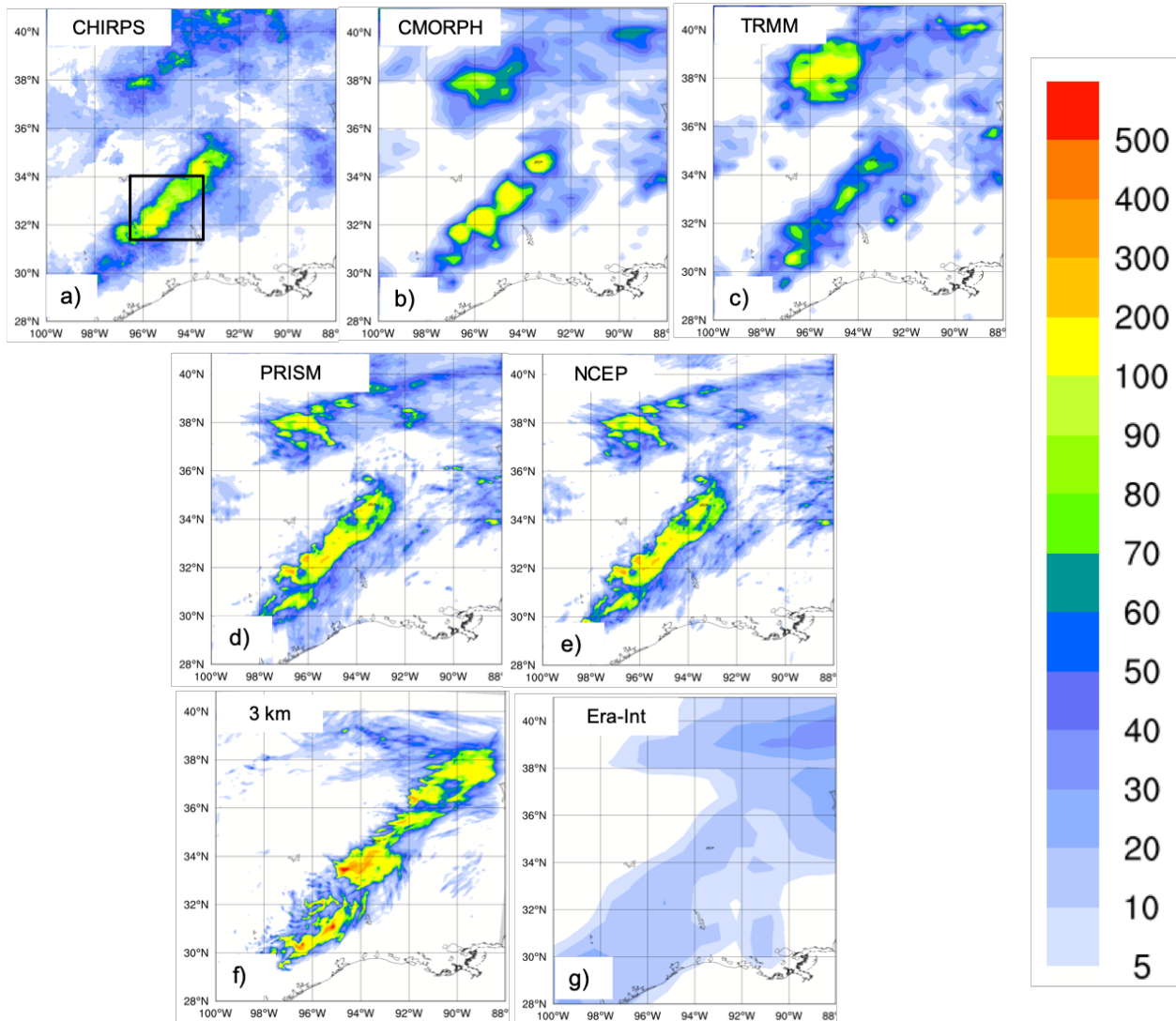
470

471 **Figure 7: Total accumulated precipitation (mm) during the Texas case: CHIRPS (a),**

472 **CMORPH (b), TRMM (c), PRISM (d), NCEP Reanalysis (e) and convection-permitting**

473 **simulation with RegCM4-NH at 3 km grid spacing (f) and ERA-Interim (g). The black box (a)**

474 **shows the area where the spatial average of 6-hourly accumulated precipitation was**

475 **calculated for Figure 6b**

476 As for the California case, the observed precipitation datasets show coherent patterns for

477 the total accumulated precipitation (Figure 7), with the highest values related to the

478 mesoscale convective system in eastern Texas (~ 200 mm), and another smaller area of

479 high precipitation more to the north, approximately over Oklahoma. PRISM (Figure

480 7d)and NCEP (Figure 7e) capture similar spatial details and magnitudes of extremes,

481 CHIRPS (Figure 7a) has lower precipitation extremes in the north compared to the other

482 datasets, while CMORPH (Figure 7b) and TRMM (Figure 7c) show the lowest

483 precipitation extremes and reduced spatial details as already noted for the California

484 case.

485 Figure 7f and Figure 7g present precipitation as produced by the RegCM4-NH and the

486 ERA-Interim reanalysis (driving data) respectively. ERA-Interim reproduces some of the

487 observed features of precipitation, but with a substantial underestimation over the areas

488 of maximum precipitation because of its coarse resolution. By comparison, the RegCM4-

489 NH simulation (Fig. 7f) shows an improvement in both pattern and intensity of

490 precipitation, and is substantially closer to observations over eastern Texas. However,

491 the precipitation area is slightly overestimated and the model is not capable of

492 reproducing the small region of maximum precipitation in the north.

493

494 The time series of precipitation over eastern Texas from June 9 to 12, 2010 for

495 observations (black line), ERA-Interim (blue line) and RegCM4-NH (red line) are reported

496 in figure 6b. Precipitation increases over this region from 0000 UTC until it reaches the

497 observed maximum at 1200 UTC, on June 10 (~35 mm), gradually decreasing afterwards

498 until 0600 UTC, on June 11. The RegCM4-NH simulation shows a more realistic temporal

499 evolution than the ERA-Interim, which exhibits an overall underestimation of precipitation.

500 The non-hydrostatic model produces precipitation values closer to the observations,

501 however the simulated maximum is reached 6 hours earlier than observed.

502

503

504 **Lake Victoria**

505 Case 3 focuses on Lake Victoria (LKV), with the purpose of testing RegCM4-NH on a

506 complex and challenging region in terms of convective rainfall. It is estimated that each

507 year 3,000-5,000 fishermen perish on the lake due to nightly storms (Red Cross, 2014).

508 In the Lake Victoria basin, the diurnal cycle of convection is strongly influenced by

509 lake/land breezes driven by the thermal gradient between the lake surface and the

510   surrounding land. As the land warms during the course of the day, a lake breeze is
511   generated which flows from the relatively cooler water towards the warmer land surface.
512   The circulation is effectively reversed at night, when the land surface becomes cooler
513   than the lake surface, leading to convergence over the lake and associated thermal
514   instability.

515   In the LKV region, prevailing winds are generally easterly most of the year with some
516   variability due to the movement of the ITCZ. The local diurnal circulation created by the
517   presence of the lake creates two diurnal rainfall maxima. During daylight hours, when the
518   lake breeze begins to advance inland, convergence is maximized on the eastern coast of
519   the lake as the lake breeze interacts with the prevailing easterlies. Studies have also
520   noted the importance of downslope katabatic winds along the mountains to the east of
521   the lake in facilitating convergence along the eastern coastal regions (Anyah et al. 2006).
522   This creates a maximum in rainfall and convection on the eastern coast of LKV.
523   Conversely, during nighttime hours, when the local lake circulation switches to flow from
524   the land towards the lake, the prevailing easterlies create locally strong easterly flow
525   across the lake and an associated maximum in convergence and rainfall on the western
526   side of LKV.

527   The LKV simulation starts on November 25, 1999 and extends to the beginning of
528   December 1999 (Table 2), covering a 5-day period which falls within the short-rain season
529   of East Africa. The choice of 1999, an ENSO neutral year, was made in order to focus the
530   analysis on local effects, such as the diurnal convection cycle in response to the lake/land
531   breeze, with no influence of anomalous large scale conditions. A 1-dimensional lake
532   model (Hostetler et al. 1993; Bennington et al. 2014) interactively coupled to RegCM4-
533   NH was utilized to calculate the lake surface temperature (LST), since lake-atmosphere
534   coupling has been shown to be important for LKV (Sun et al. 2015; Song et al. 2004).
535   This coupled lake model has been already used for other lakes, including Lake Malawi in
536   southern Africa (Diallo et al. 2018). As with the other experiments, the boundary
537   conditions are provided by a corresponding 12 km RegCM4 simulation employing the
538   convection scheme of Tiedtke (1996).

539   At the beginning of the simulation, the LST over the lake is uniformly set to 26°C, and is
540   then allowed to evolve according to the lake-atmosphere coupling. This initial LST value
541   is based on previous studies. For example, Talling (1969) finds Lake Victoria surface
542   temperatures ranging from 24.5-26°C during the course of the year. Several studies have
543   used RCMs to investigate the Lake Victoria climate (Anyah et al., 2006; Anyah and
544   Semazzi 2009, Sun et al. 2015), and found a significant relationship between lake
545   temperature and rainfall depending on season. The value of 26°C is typical of the winter
546   season and was chosen based on preliminary sensitivity tests using different values of
547   initial temperature ranging from 24°C to 26°C.

548   The synoptic feature favorable for the production of precipitation over the LKV in this
549   period corresponds to a large area of southeasterly flow from the Indian Ocean (Fig. 8a),
550   which brings low-level warm moist air into the LKV region facilitating the production of
551   convective instability and precipitation. This synoptic situation, with a low-level south-
552   easterly jet off the Indian Ocean, is a common feature associated with high precipitation
553   in the area (Anyah et al. 2006), and can be seen in ERA5 data (Figure 8a). Although
554   some bias in terms of magnitude, this is reasonably well reproduce by the 12 km
555   simulation (Figure 8b).

556
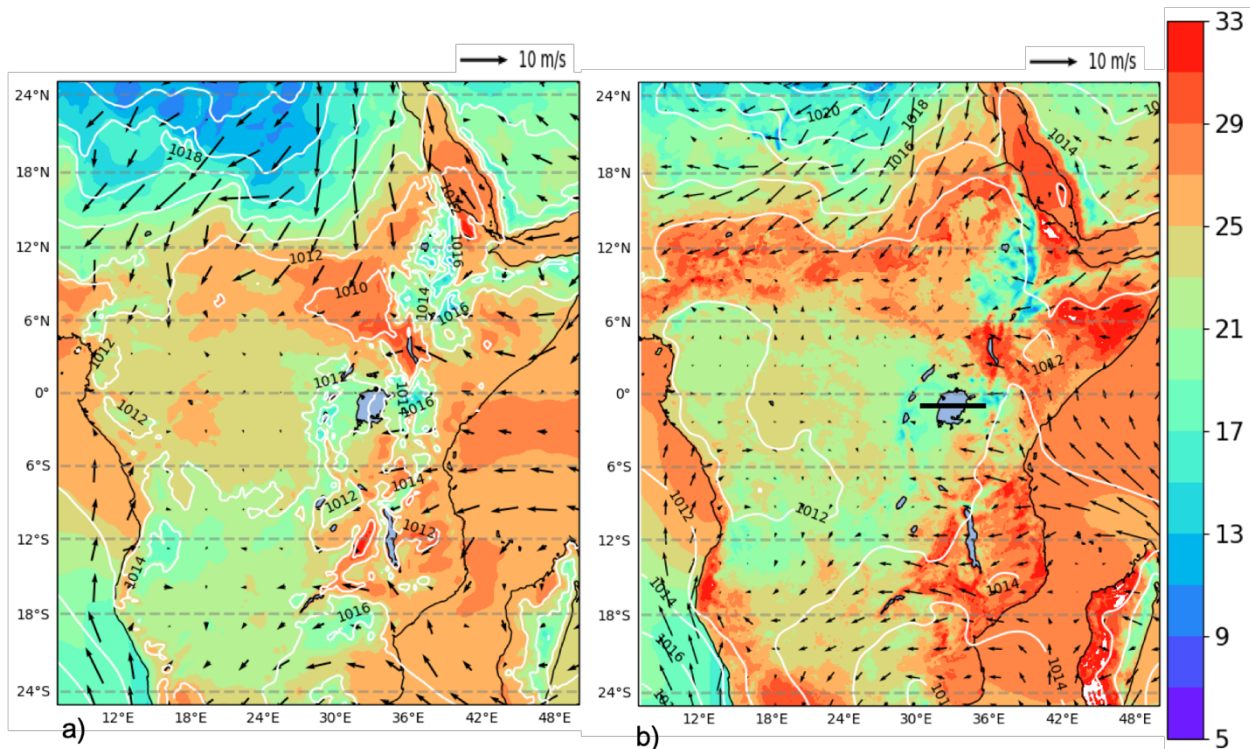
Figure 8: Mean sea level pressure (mslp) (hPa) (white contour lines), surface temperature (color shading) (°C) and 100-m wind (black arrows) averaged over the period 25 November 0000 UTC - 1 December 0000 UTC, by ERA5 reanalysis (a) and RegCM 12km (b). The black line (b) shows the cross-section position represented in Fig. 9

The LKV region dynamics are quite distinct between nighttime and daytime and the rainfall in and around the lake has a pronounced diurnal cycle. To understand this strong diurnal cycle, Figure 9 shows a cross-section through the lake (32E to 34E, black line in right panel of Fig. 8b) along 1°S latitude at a period during strong nighttime (Fig. 9b,d; 0600Z November 30) and daytime convection (Figure 9a,c; 12Z November 29). Wind vectors in Figure 9 show the zonal-wind anomaly across 0°-2°S to highlight the circulations associated with LKV. During the day, surface heating around the lake leads to a temperature difference between the land and lake sufficient to generate a lake breeze, which causes divergence over the lake, while over the highlands to the east the environment is more conducive to convection where convergence is focused (9a,c). Conversely, during the night, a land breeze circulation is generated, which induces convergence and convection over the lake (Figure 9b,d). In Figure 10, the evolution of

573   the nighttime land breeze is illustrated with cooler temperature anomalies propagating
574   westward onto the lake during the night.

575   Comparing the 3 km simulation to the 12 km forcing run, we find that the localized
576   circulations created by local forcings (i.e. convection) are much stronger in the convection
577   permitting resolution experiment. We also find stronger and more localized areas of
578   convective updrafts compared to the 12 km simulation (Figure 9c,d; omega is shown
579   instead of vertical velocity here because of the difference in dynamical core). As an
580   example during the nighttime event (Figure 9b,d) there is a broad area of upward motion
581   over the lake and the associated broad convergence in the 12km simulation, while in the
582   convection permitting 3km simulation, convection is much more local and concentrated
583   over the western part of the lake. Indeed, nighttime rainfall tends to be concentrated over
584   the western part of the lake (Sun et al. 2015; Figure 11a-d). Stronger convection
585   simulated in the 3 km experiment could also be tied to stronger temperature anomalies
586   shown over the lake and land and between day and night relative to the 12km simulation
587   (Figure 10). The 3km simulation also shows a more pronounced land breeze propagation
588   at night compared to the 12km simulation.

589   This demonstrates that the 3km simulation is better equipped to simulate the localized
590   circulations associated with this complex land-lake system.

591     $15\overrightarrow{} \text{ms}^{-1}$

592
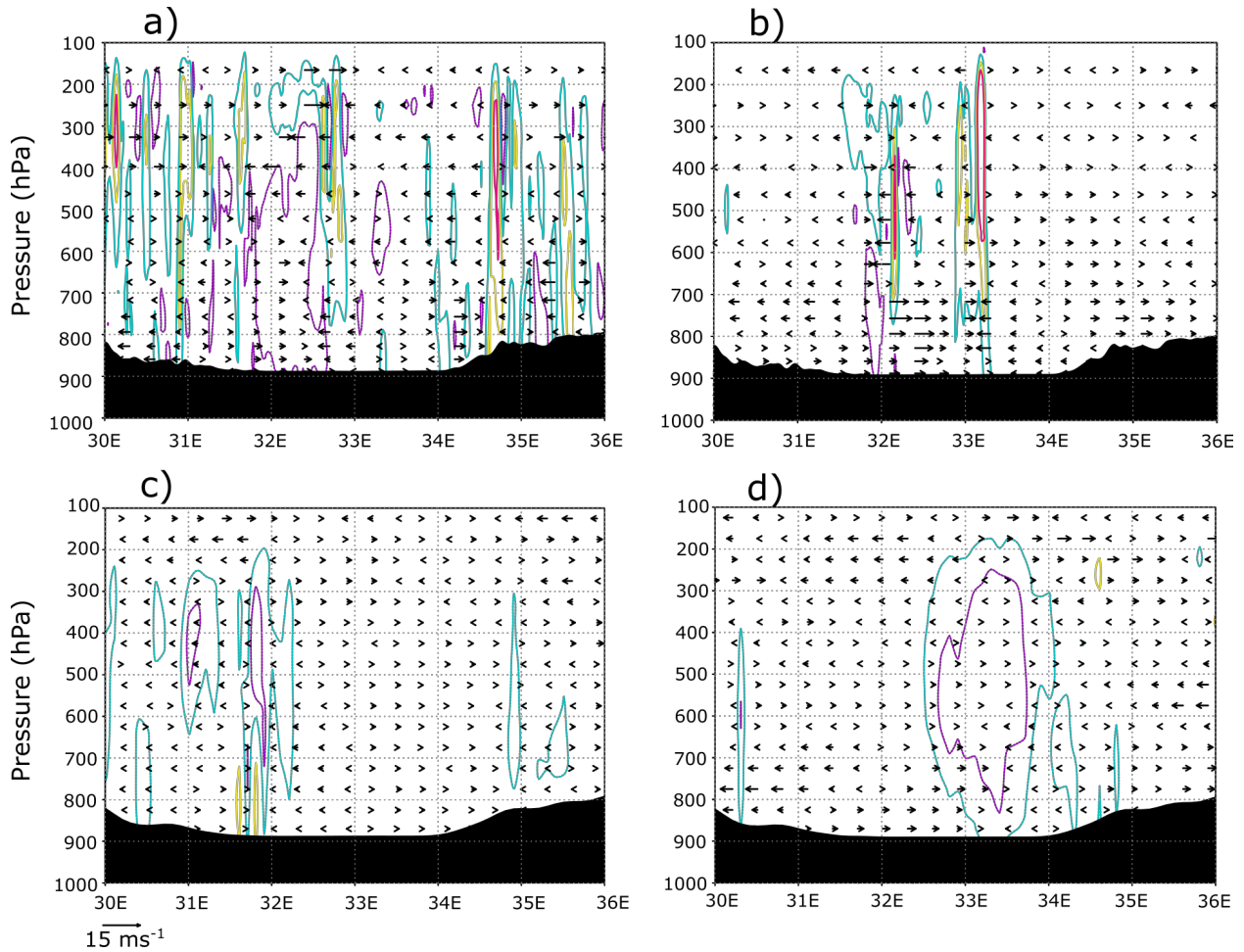
Figure 9. Cross-section through 1°S (black line in Fig. 8b) of the zonal-wind anomaly (0°-2°S) vectors and the mean contoured vertical velocity (m/s) over 0°-2°S at a) 12Z 29 November and b) 6Z 30 November from the 3km simulation. Purple dashed contours indicate -0.1 m/s, light blue contours indicate 0.1 m/s, yellow contours indicate 0.3 m/s, and red contours indicate 0.5 m/s. Lake Victoria encompasses about 32°E to 34°E. The bottom 2 panels show the same as in a) and b) but from the 12km simulation at c) 12Z 29 November and d) 6Z 30 November. Purple dashed contours indicate -0.01 hPa/s, light blue dashed contours indicate -0.005 hPa/s, and yellow dashed contours indicate 0.005 hPa/s.

601
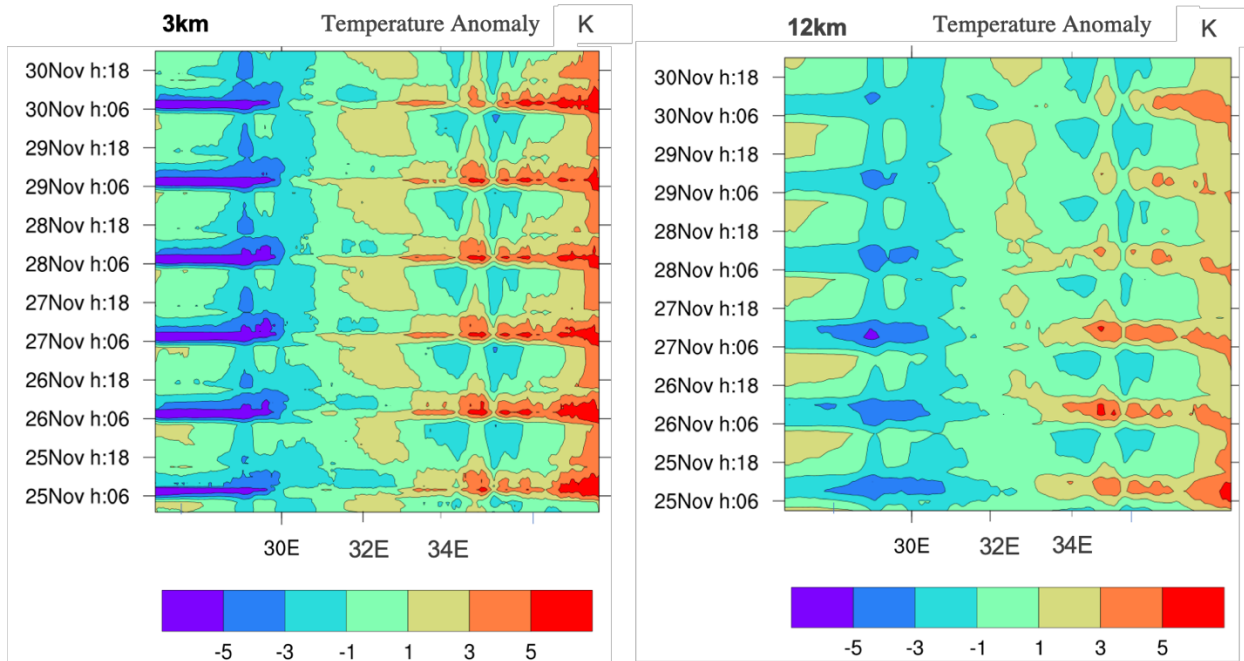
Figure 10 : **Longitude-time (hourly) Hovmöller diagram of LKV domain surface temperature anomaly (shading, in K). Panels correspond to the 3km simulation (left) and 12km simulation (right). The lake Victoria is between 32°E and 34°E longitude**

607
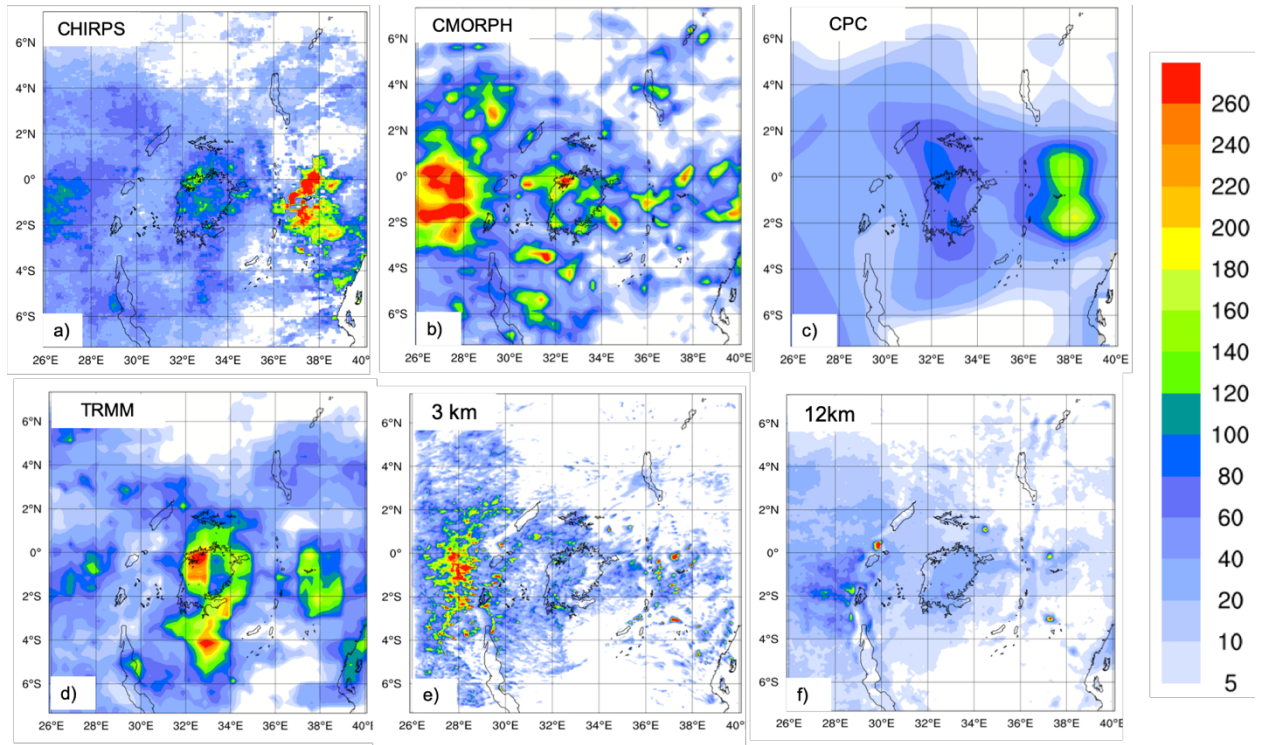
Figure 11: Total event accumulated precipitation (mm) during the LKV case (November 25, 1999-December 1, 1999) measured by CHIRPS (a), CMORPH (b), CPC (d) TRMM (e) and calculated by RegCM4 at 3 km (e) and 12 km (f).

611

Figure 11 reports the total accumulated precipitation observed and simulated for the LKV case. TRMM (Figure 11d) and CPC (Figure 11c) show a similar pattern, with two-rainfall maxima of different intensities over the southeastern and northwestern lake areas. CMORPH (Figure 11b) shows a western rainfall maximum similar to TRMM and one large rainfall area almost entirely centered over the highlands to the west of the lake. Conversely in CHIRPS (Figure 11a) a maximum is found to the east of the lake while several localized maxima occur over the lake. The differences among the observed datasets highlight the issue of observational uncertainty and the need to take into consideration shortcomings associated with the types of observational datasets considered. Different datasets can have significantly different climatologies, especially in areas of low data availability. For example, Prein and Gobiet (2017) analyzed two gauge-based European-wide datasets, and seven global low-resolution datasets, and found

624   large differences across the observation products, often of similar magnitude as the
625   difference among model simulations. In this case and for this area the observation
626   uncertainty plays a big role especially at high resolution, and highlights the need for an
627   adequate observational network for model validation. However, despite the large
628   uncertainty among the different observed datasets (Figure 11 a-d), we find a significant
629   underestimation of the precipitation by the 12 km run over the lake independently of the
630   dataset used as a reference (Figure11f). In contrast, the 3 km simulation (Figure 11e)
631   shows substantially greater detail, with rainfall patterns more in agreement with the
632   CMORPH data. In particular, the 3 km simulation reproduces well the local rainfall
633   maxima on the western side of the lake, although these appear more localized and with
634   a multi-cell structure compared to CMORPH and TRMM. Additionally, the 12 km
635   simulation underestimates the observed heavy rainfall totals in the highlands to the west
636   of the lake region especially when compared to CMORPH, which are instead reproduced
637   by the 3 km simulation.

638   This last test case demonstrates the ability of RegCM4-NH in simulating realistic
639   convective activity over a such morphologically complex region, which is a significant
640   improvement compared to the hydrostatic-coarse resolution model configuration.

641

642   **Conclusions and future outlook**

643

644   In this paper we have described the development of RegCM4-NH, a non hydrostatic
645   version of the regional model system RegCM4, which was completed in response to the
646   need of moving to simulations at convection-permitting resolutions of a few kilometers.
647   The non-hydrostatic dynamical core of MM5 has been incorporated into the RegCM4
648   system previously based on the MM5 hydrostatic core. Some modifications to the MM5
649   dynamical core were also implemented to increase the model stability for long term runs.
650   RegCM4-NH also includes two explicit cloud microphysics schemes needed to explicitly
651   describe convection and cloud processes in the absence of the use of cumulus
652   convection schemes. Finally, we presented a few case studies of explosive convection to

653   illustrate how the model provides realistic results in different settings and general

654   improvements compared to the coarser resolution hydrostatic version of RegCM4 for

655   such types of events.

656

657   As already mentioned, RegCM4-NH is currently being used for different projects, and

658   within these contests, is being run at grid spacings of a few kilometers for continuous

659   decadal simulations, driven by reanalyses of observations or GCM boundary conditions

660   (with the use of an intermediate resolution domains) over different regions, such as the

661   Alps, the Eastern Mediterranean, Central-Eastern Europe and the Caribbeans. These

662   projects, involving multi-model inter-comparisons, indicate that the performance of

663   RegCM4-NH is generally in line with that of other convection-permitting models, and

664   exhibits similar improvements compared to coarser resolution models, such as a better

665   simulation of the precipitation diurnal cycle and of extremes at hourly to daily time scales.

666   The results obtained within the multi-model context confirm previous results from single-

667   model studies (Kendon et al. 2012, 2017, Ban et al. 2014, 2015; Prein et al. 2015, 2017),

668   but also strengthen the robustness of the findings through reduced uncertainty compared

669   to coarse resolution counterpart (Ban et al., 2021, Pichelli et al., 2021). The convection-

670   permitting scale can thus open the perspective of more robust projections of future

671   changes of precipitation, especially over sub-daily time scales.

672

673   One of the problems of the RegCM4-NH dynamical core is that, especially for long runs

674   with varied meteorological conditions, a relatively short time step is needed for stability

675   reasons. This makes the model rather computationally demanding, although not more

676   than other convection-permitting modeling systems such as the Weather Research and

677   Forecast model (WRF, Skamarok et al. 2008). For this reason, we are currently

678   incorporating within the RegCM system a very different and more computationally efficient

679   non-hydrostatic dynamical core, which will provide the basis for the next version of the

680   model, RegCM5, to be released in the future.

681

682   Following the philosophy of the RegCM modeling system, RegCM4-NH is intended to be

683   a public, free, open source community resource for external model users. The non-

684   hydrostatic dynamical core has been implemented in a way that it can be activated in

685   place of the hydrostatic dynamics through a user-set switch, which makes the use of

686   RegCM4-NH particularly simple and flexible. We therefore envision that the model will be

687   increasingly used by a broad community so that a better understanding can be achieved

688   of its behavior, advantages and limitations.

689

690   **Code availability**: https://zenodo.org/record/4603556

691   **Cases study configuration files:** https://zenodo.org/record/5106399

692

693

694   **Author contribution**: CE prepared the manuscript with contributions from all co-authors

695   and coordinated research, SP, TA, GR carried out and analysed the simulations, PE

696   investigated solutions to stabilize/adapt the model at the km-scale and performed

697   preliminary validation tests, GG developed/adapted the model code, FDS contributed to

698   develop the coupled version of the model, NR developed one of the microphysics

699   scheme, GF supervised and coordinated all activities.

700

701   **Competing interests**: The authors declare that they have no conflict of interest.

702

703

704   References

705   Anthes, R. A., Hsie, E. -Y., and Kuo, Y. -H.: Description of the Penn State/NCAR

706   Mesoscale Model: Version 4 (MM4) (No. NCAR/TN-282+STR), doi:10.5065/D64B2Z90,

707   1987.

708   Anyah R.O. and Semazzi F.: Idealized simulation of hydrodynamic characteristics of Lake

709   Victoria that potentially modulate regional climate, Int. J. Climatol. 29(7):971–981.

710   doi:10.1002/joc.1795, 2009.

711   Anyah, R., Semazzi, F. H. M. and Xie, L.: Simulated Physical Mechanisms Associated

712   with Climate Variability over Lake Victoria Basin in East Africa, Mon. Wea. Rev., 134

713   3588-3609, 2006.

714 Ashouri, H., Hsu, K., Sorooshian, S., Braithwaite, D. K., Knapp, K. R., Cecil, L. D., Nelson,

715 B. R. and Prat, O. P.: PERSIANN-CDR: Daily Precipitation Climate Data Record from

716 Multisatellite Observations for Hydrological and Climate Studies, Bulletin of the American

717 Meteorological Society, *96*(1), 69-83, doi : 10.1175/BAMS-D-13-00068.1, 2015.

718

719 Ban, N., Schmidli, J., and Schär ,C.: Evaluation of the convection-resolving regional

720 climate modeling approach in decade-long simulations, J. Geophys. Res. Atmos., 119,

721 7889– 7907, https://doi.org/10.1002/2014JD021478, 2014.

722

723 Ban, N., Schmidli, J., and Schär ,C.: Heavy precipitation in a changing climate: does short-

724 term summer precipitation increase faster?, Geophys Res Lett 42:1165–1172.

725 https://doi.org/10.1002/2014G L062588, 2015

726

727 Ban, N., Caillaud, C., Coppola, E. et al.: The first multi-model ensemble of regional climate

728 simulations at kilometer-scale resolution, part I: evaluation of precipitation, *Clim Dyn* .

729 https://doi.org/10.1007/s00382-021-05708-w, 2021.

730

731 Beheng, K.: A parameterization of warm cloud microphysical conversion processes,

732 Atmos. Res., 33, 193–206, 1994

733

734 Bennington, V., Notaro, M. and Holman, K.D.: Improving Climate Sensitivity of Deep

735 Lakes within a Regional Climate Model and Its Impact on Simulated Climate, J. Climl, 27,

736 2886-2911, 2014.

737

738 Bretherton, C.S., McCaa, J.R., and Grenier, H.: A new parameterization for shallow

739 cumulus convection and its application to marine subtropical cloud-topped boundary lay-

740 ers. I. Description and 1D results, Mon Weather Rev 132: 864– 882, 2004.

741

742 Chan, S. C., Kendon, E. J., Fowler, H. J., Blenkinsop, S., Roberts, N. M. and Ferro,

743 C.A.T.: The value of high- resolution Met Office regional climate models in the simulation

of multi-hourly precipitation extremes, J. Climate, 27, 6155–6174, https://doi.org/10.1175/JCLI-D-13-00723.1, 2014.

Chen, M. and Xie, P.: CPC Unified Gauge-based Analysis of Global Daily Precipitation, *2008 Western Pacific Geophysics Meeting*. ISBN: 0026- 0576. DOI: http://dx.doi.org/10.1016/S0026-0576(07)80022-5, 2008.

Clark, P., Roberts, N., Lean, H. , Ballard, S. P. and Charlton- Perez, C.: Convection-permitting models: A step-change in rainfall forecasting, Meteor. Appl., 23, 165–181, https://doi.org/ 10.1002/met.1538, 2016.

Coppola, E., Sobolowski, S., Pichelli, E. et al. A first-of-its-kind multi-model convection permitting ensemble for investigating convective phenomena over Europe and the Mediterranean. Clim Dyn 55, 3–34, https://doi.org/10.1007/s00382-018-4521-8, 2020.

Coppola, E., Giorgi, F., Mariotti, L. and Bi, X.: RegT-Band: a tropical band version of RegCM4, Clim Res 52: 115–133, 2012.

Dacre, H. F., Clark, P. A., Martinez-Alvarado, O., Stringer, M. A. and Lavers, D. A.: How do atmospheric rivers form?, Bull. Amer. Meteor. Soc., 96, 1243-1255, https://doi.org/10.1175/BAMS-D-14-00031, 2015.

Dale, M., Hosking, A., Gill, E., Kendon, E. J., Fowler, H. J., Blenkinsop, S. and Chan, S. C.: Understanding how changing rainfall may impact on urban drainage systems; lessons from projects in the UK and USA, Water Pract. Technol., 13, 654–661, https://doi.org/10.2166/wpt.2018.069, 2018.

Diallo, I., Giorgi, F. and Stordal, F.: Influence of Lake Malawi on regional climate from a double nested regional climate model experiment, Climate Dynamics, 50, 3397– 3411. https://doi.org/10.1007/s00382-017-3811-x, 2018.

775 Dickinson, R.E., Errico, R.M., Giorgi, F. et al.: A regional climate model for the western
776 United States, Climatic Change 15, 383–422 (1989),
777 https://doi.org/10.1007/BF00240465, 2018.
778
779 Dickinson, R.E., Henderson-Sellers, A. and Kennedy, P.: Bio -sphere– atmosphere
780 transfer scheme (BATS) version 1eas coupled to the NCAR community climate model,
781 TechRep, National Center for Atmospheric Research TechNote NCAR.TN-387+ STR,
782 NCAR, Boulder, CO, 1993.
783
784 Done, J., Davis, C. A. and Weisman M. L.: The next gener- ation of NWP: Explicit
785 forecasts of convection using the Weather Research and Forecasting (WRF) model,
786 Atmos. Sci. Lett., 5, 110–117, https://doi.org/10.1002/asl.72, 2004.
787
788 Dudhia, J.: Numerical study of convection observed during the winter monsoon
789 experiment using a mesoscale two-dimensional model, J. Atmos. Sci., 46, 3077–3107,
790 1989.
791
792 Durran, D.R. and Klemp, J.B.: A compressible model for the simulation of moist mountain
793 waves, Mon. Wea. Rev., 111, 2341–236, 1983.
794
795 Elguindi, N., Bi, X., Giorgi, F. , Nagarajan, B., Pal J., Solmon, F., Rauscher, S., Zakey,
796 S., O'Brien, T., Nogherotto, R. and Giuliani, G.: Regional Climate Model RegCM
797 Reference Manual Version 4.7, 49 pp, https://zenodo.org/record/4603616, 2017.
798
799 Emanuel, K.A.: A scheme for representing cumulus convection in large-scale models, J.
800 Atmos. Sci, 48, 2313–2335, 1991.
801
802 Fairall, C.W., Bradley, E.F., Godfrey, J.S. , Wick, G.A., Edson, J.B. and Young, G.S.: The
803 cool skin and the warm layer in bulk flux calculations, J. Geophys. Res., 101, 1295-1308,
804 1996a.
805

806 Fairall, C.W., Bradley, E.F., Rogers, D.P., Edson, J.B. and Young, G.S.: Bulk
807 parameterization of air-sea fluxes for TOGA COARE, J. Geophys. Res., 101, 3747-3764,
808 1996b.

810 Funk, C., Peterson, P., Landsfeld, M. et al. The climate hazards infrared precipitation with
811 stations—a new environmental record for monitoring extremes, Sci Data 2, 150066,
812 https://doi.org/10.1038/sdata.2015.66, 2015.

814 Gimeno, L., Nieto, R., Vàsquez, M. and Lavers, D. A.: Atmospheric rivers: A mini-review,
815 Front. Earth Sci., 2, https://doi.org/10.3389/feart.2014.00002, 2014.

817 Giorgi F.: Thirty years of regional climate modeling: where are we and where are we going
818 next?, J Geophys Res Atmos 124:5696–5723, 2019.

820 Giorgi, F., Coppola, E., Solmon, F., Mariotti, L. et al.: RegCM4: model description and
821 preliminary tests over multiple CORDEX domains, Clim Res 52:7-29.
822 https://doi.org/10.3354/cr01018, 2012.

824 Giorgi, F., Francisco, R. and Pal, J.S.: Effects of a sub-gridscale topography and landuse
825 scheme on surface climateand hydrology. I. Effects of temperature and water vapor
826 disaggregation, J Hydrometeorol., 4, 317– 333, 2003.

828 Giorgi, F., Jones, C. and Asrar, G.: Addressing climate information needs at the regional
829 level: the CORDEX framework, WMO Bull, 175–183, 2009.

831 Giorgi, F. and Mearns, L.O.: Introduction to special section: regional climate modeling
832 revisited, J Geophys Res, 104, 6335–6352, 1999.

834 Giorgi, F., Marinucci, M.R. and Bates, G.: Development of a second generation regional
835 climate model (RegCM2). I. Boundary layer and radiative transfer processes, Mon
836 Weather Rev., 121, 2794–2813, 1993a.

837   Giorgi, F., Marinucci, M.R., Bates, G. and De Canio, G.: Development of a second
838   generation regional climate model (RegCM2), part II: convective processes and
839   assimilation of lateral boundary conditions, Mon. Weather Rev., 121, 2814–2832, 1993b.
840

841   Giorgi, F., and Bates, G.T.: The Climatological Skill of a Regional Model over Complex
842   Terrain, Mon. Wea. Rev., 117, 2325–2347, https://doi.org/10.1175/1520-
843   0493(1989)117<2325:TCSOAR>2.0.CO;2, 1989.
844

845   Grell, G.A.: Prognostic evaluation of assumptions used by cumulus parameterizations,
846   Mon. Weather Rev. 121, 764– 787, 1993.
847

848   Grell, G.A., Dudhia J. and Stauffer, D. R.: A Description of the Fifth Generation Penn
849   State/NCAR Mesoscale Model (MM5), NCAR Tech. Note, NCAR/TN-398+ STR, Boulder,
850   p. 122, 1994.
851

852   Gunn, K. L. S., and Marshall, J. S. : The distribution with size of aggregate snowflakes, J.
853   Meteor., 15, 452–461, https://doi.org/10.1175/1520-
854   0469(1958)015<0452:TDWSOA>2.0.CO;2, 1958.
855

856   Gutowski Jr., W. J., Giorgi, F., Timbal, B., Frigon, A., Jacob, D., Kang, H.-S., Raghavan,
857   K., Lee, B., Lennard, C., Nikulin, G., O'Rourke, E., Rixen, M., Solman, S., Stephenson,
858   T., and Tangang, F.: WCRP COordinated Regional Downscaling EXperiment (CORDEX):
859   a diagnostic MIP for CMIP6, Geosci. Model Dev., 9, 4087–4095,
860   https://doi.org/10.5194/gmd-9-4087-2016, 2016.
861

862   Holtslag, A., de Bruijn, E. and Pan, H.L.: A high resolution air mass transformation model
863   for short-range weather fore-casting, Mon Weather Rev 118: 1561–1575, 1990.
864

865   Hostetler, S.W., Bates, G.T. and Giorgi, F.: Interactive nesting of a lake thermal model
866   within a regional climate model for climate change studies, J Geophys Res 98: 5045–
867   5057, 1993.

868   Huffman, G. J., Bolvin, D. T., Nelkin, E. J., Wolff, D. B., Adler, R. F., Gu, G., Hong, Y.,

869   Bowman, K. P. and Stocker, E. F.: The TRMM Multisatellite Precipitation Analysis

870   (TMPA): Quasi-global, multiyear, combined-sensor precipitation estimates at fine scales,

871   J. Hydrometeor., 8, 38–55, doi:https://doi.org/10.1175/JHM560.1, 2007.

872

873   Kiehl, J., Hack, J., Bonan, G., Boville, B., Breigleb, B., Williamson, D. and Rasch, P.:

874   Description of the NCAR Commun -ity Climate Model (CCM3), National Center for

875   Atmospheric Research Tech Note NCAR/TN-420+ STR, NCAR, Boulder, CO, 1996.

876

877   Lean, H. W., Clark, P. A., Dixon, M., Roberts, N. M., Fitch, A., Forbes, R. and Halliwell,

878   C.: Characteristics of high-resolution versions of the Met Office Unified Model for

879   forecasting convection over the United Kingdom, Mon. Wea. Rev., 136, 3408–3424,

880   https://doi.org/10.1175/2008MWR2332.1, 2008.

881

882   Lind, P., Lindstedt, D., Kjellstrom, E. and Jones, C.: Spatial and temporal characteristics

883   of summer precipitation over central Europe in a suite of high-resolution climate models,

884   J. Climate, 29, 3501–3518, https://doi.org/10.1175/JCLI-D-15- 0463.1, 2016.

885

886   Hewitt, C. D. and Lowe, J. A.: Toward a European climate prediction system, Bull. Amer.

887   Meteor. Soc., 99, 1997–2001, https://doi.org/10.1175/BAMS-D-18-0022.1, 2018.

888

889   Hong, S.-Y., Juang, H.-M. H. and Zhao, Q.: Implementation of prognostic cloud scheme

890   for a regional spectral model, Mon. Wea. Rev., 126, 2621–2639, 1998.

891

892   Hong, S.-Y., Dudhia, J. and Chen, S.-H.: A Revised Approach to Ice Microphysical

893   Processes for the Bulk Parameterization of Clouds and Precipitation, Mon. Wea. Rev.,

894   132, 103–120, 2004.

895

896   Hong, S.-Y., and Lim, J.-O. J.: The WRF Single-Moment 6-Class Microphysics Scheme

897   (WSM6), J. Korean Meteor. Soc., 42, 129–151, 2006.

898

Hostetler, S.W., Bates, G.T. and Giorgi, F.: Interactive Coupling of Lake Thermal Model with a Regional climate Model, J. Geophys. Res., 98(D3), 5045-5057, 1993.

Huffman, G. J., Bolvin, D. T., Nelkin, E. J., Wolff, D. B., Adler, R. F., Gu, G., Hong, Y., Bowman, K. P. and Stocker, E. F.: The TRMM Multisatellite Precipitation Analysis (TMPA): Quasi-Global, Multiyear, Combined-Sensor Precipitation Estimates at Fine Scales, Journal of Hydrometeor., 8(1), 38-55, DOI: 10.1175/JHM560.1, 2007.

Joyce, R. J., Janowiak, J. E., Arkin, P. A. and Xie, P.: CMORPH: A Method that Produces Global Precipitation Estimates from Passive Microwave and Infrared Data at High Spatial and Temporal Resolution. J. Hydrometeor, 5(3), 487–503, 2004.

Kain, J. S.: The Kain–Fritsch convective parameterization: An update, J. Appl. Meteor., 43, 170–181, https://doi.org/10.1175/1520-0450(2004)043<0170:TKCPAU>2.0.CO;2, 2004.

Kain, J. S. and Fritsch, J. M.: A one-dimensional entraining/ detraining plume model and its application in convective parameterization, J. Atmos. Sci., 47, 2784–2802, 1990.

Kendon, E. J., Roberts, N. M., Senior, C. A. and Roberts, M. J.: Realism of rainfall in a very high-resolution regional climate model, J. Climate, 25, 5791–5806, https://doi.org/ 10.1175/JCLI-D-11-00562.1, 2012.

Kendon, E. J., Ban, N., Roberts, N. M., Fowler, H. J., Roberts, M. J., Chan, S. C., Evans, J. P., Fosser, G. and Wilkinson, J. M.: Do convection-permitting regional climate models improve projections of future precipitation change?, Bull. Amer. Meteor. Soc., 98, 79–93, https://doi.org/ 10.1175/BAMS-D-15-0004.1, 2017.

Kessler, E.: On the Distribution and Continuity of Water Substance in Atmospheric Circulations, Meteor. Monogr., No. 32, Amer. Meteor. Soc., 84 pp, 1969.

930   Khairoutdinov, M. and Kogan, Y.: A new cloud physics parameterization in a large-eddy
931   simulation model of marine stratocumulus, Bull. Amer. Meteorol. Soc., 128, 229–243,
932   2000

933

934   Klemp, J.B. and Dudhia, J.: An Upper Gravity-Wave Absorbing Layer for NWP
935   Applications, Monthly Weather Review, 176, 3987-4004, 2008.

936

937   Klemp, J. B. and Lilly, D. K.: Numerical simulation of hydrostatic mountain waves, J.
938   Atmos. Sci., 35, 78–107, 1978.

939

940   Lin, Y., Farley, R. and Orville, H.: Bulk parameterization of the snow field in a cloud model,
941   J. Appl. Meteor. Clim., 22, 1065–1092, 1983.

942

943   Marshall, J. S. and Palmer, W. M. K.: The distribution of raindrops with size. J. Meteor.,
944   5, 165–166, 1948.

945

946   Matte, D., Laprise, R., Thériault, J. M. and Lucas-Picher, P.: Spatial spin-up of fine scales
947   in a regional climate model simulation driven by low-resolution boundary conditions.
948   Climate Dynamics, *49(1-2), 563–574.* doi:10.1007/s00382-016-3358-2, 2017.

949

950   Mlawer, E. J., Taubman, S. J., Brown, P. D., Iacono, M. J. and Clough, S. A.: Radiative
951   transfer for inhomogeneous atmospheres: RRTM, a validated correlated-k model for the
952   longwave, J. Geophys. Res., 102, 16663-16682, 1997.

953

954   Nogherotto, R., Tompkins, A.M., Giuliani, G., Coppola, E. and Giorgi, F.: Numerical
955   framework and performance of the new multiple-phase cloud microphysics scheme in
956   RegCM4. 5: precipitation, cloud microphysics, and cloud radiative effects. Geoscientific
957   Model Development, 9(7), 2533-2547, 2016.

958

959   Oleson, K. W., Lawrence, D. M., Bonan, G. B., Drewniak, B., Huang, M., Koven, C. D.,

960   Levis, S., Li, F., Riley, W. J., Subin, Z. M., Swenson, S. C., Thornton, P. E., Bozbiyik, A.,

961   Fisher, R., Kluzek, E., Lamarque, J. -F., Lawrence, P. J., Leung, L. R., Lipscomb, W.,

962   Muszala, S., Ricciuto, D. M., Sacks, W., Sun, Y., Tang, J., and Yang, Z. -L:Technical

963   Description of version 4.5 of the Community Land Model (CLM),Ncar Technical Note

964   NCAR/TN-503+STR, National Center for Atmospheric Research, Boulder, CO, 422 pp,

965   DOI: 10.5065/D6RR1W7M, 2013.

966

967   Pal, J.S., Small, E. and Eltahir, E.: Simulation of regional-scale water and energy

968   budgets: representation of subgrid cloud and precipitation processes within RegCM, J

969   Geo-phys Res 105: 29579–29594, 2000.

970

971   Pal, J. S., Giorgi, F., Bi, X., Elguindi, N., Solmon, F., Gao, X., Rauscher, S. A., Francisco,

972   R., Zakey, A., Winter, J., Ashfaq, M., Syed, F. S., Bell, J. L., Diffenbaugh, N. S.,

973   Karmacharya, J., Konaré, A., Martinez, D., da Rocha, R. P., Sloan, L. C. and Steiner, A.

974   L.: The ICTP RegCM3 and RegCNET: regional climate modeling for the developing world.

975   Bull. Amer. Meteorol. Soc., 88(9), 1395–1409, 2007.

976

977   Pichelli, E., Coppola, E., Sobolowski, S. et al.: The first multi-model ensemble of regional

978   climate simulations at kilometer-scale resolution part 2: historical and future simulations

979   of precipitation, Clim. Dyn., https://doi.org/10.1007/s00382-021-05657-4, 2021.

980

981   Prein, A. F. and Gobiet, A.: Impacts of uncertainties in European gridded precipitation

982   observations on regional climate analysis, International Journal of Climatology. ISSN:

983   10970088. DOI: 10.1002/joc.4706, 2017.

984

985   Prein, A. F., Langhans, W., Fosser, G., Ferrone, A., Ban, N., Goergen, K., Keller, M.,

986   Tölle, M., Gutjahr, O., Feser, F., et al.: A review on regional convection-permitting climate

987   modeling: demonstrations, prospects, and challenges, Rev. Geophys. 53, 323–361,

988   2015.

989

990 Ralph, F. M., Neiman, P. J., Wick, G. A., Gutman, S. I., Dettinger, M. D., Cayan, D. R.
991 and White, A. B.: Flooding on California's Russian River: Role of atmospheric rivers,
992 Geophys. Res. Lett., 33, L13801, https://doi.org/10.1029/2006GL026689, 2006.
993

994 Ralph, F. M., Dettinger, M. D., Cairns, M. M., Galarneau, T. J. and Eylander, J.: Defining
995 "atmospheric river": How the Glossary of Meteorology helped resolve a debate. Bull.
996 Amer. Meteor. Soc., 99, 837–839, https://doi.org/10.1175/BAMS-D-17-0157.1, 2018.
997

998 Rutledge, S. A. and Hobbs, P. V.: The mesoscale and microscale structure and
999 organization of clouds and precipitation in midlatitude cyclones. Part VIII: A model for the
1000 "seeder-feeder" process in warm-frontal rainbands, J. Atmos. Sci., 40, 1185–1206, 1983.
1001

1002 Skamarock, W.C., Klemp, J.B., Dudhia, J., Gill, D.O., Barker, D.M., Duda, M.G., Huang,
1003 X.Y., Wang, W. and Powers, J.G.: A description of the advanced research WRF version
1004 3, Technical Note NCAR/TN-475+STR. NCAR: Boulder, CO, 2008.
1005

1006 Schwartz, C. S.: Reproducing the September 2013 record- breaking rainfall over the
1007 Colorado Front Range with high- resolution WRF forecasts, Wea. Forecasting, 29, 393–
1008 402, https://doi.org/10.1175/WAF-D-13-00136.1, 2014.
1009

1010 Sitz, L. E., Sante, F., Farneti, R., Fuentes-Franco, R., Coppola, E., Mariotti, L., Reale, M.
1011 et al.: Description and Evaluation of the Earth System Regional Climate Model (RegCM–
1012 ES), Journal of Advances in Modeling Earth Systems. doi:10.1002/2017MS000933,
1013 2017.
1014

1015 Song, Y., Semazzi, H.M.F., Xie, L. and Ogallo, L.J.: A coupled regional climate model for
1016 the Lake Victoria Basin of East Africa, Int. J. Climatol. 24: 57-75, 2004.
1017

1018 Sun, X., Xie, L., Semazzi, F. and Liu, B.: Effect of Lake Surface Temperature on the
1019 Spatial Distribution and Intensity of the Precipitation over the Lake Victoria Basin, Mon.
1020 Wea. Rev. 143: 1179-1192, 2015.

Sundqvist, H., Berge, E. and Kristjansson, J.: Condensation and cloud parameterization studies with a mesoscale numerical weather prediction model, Mon. Weather Rev., 117, 1641–1657,1989.

Talling, J. F.: The incidence of vertical mixing, and some biological and chemical consequences, in tropical African lakes, Verh. Int. Ver. Limnol. 17, 998-1012 DOI: 10.1080/03680770.1968.11895946, 1969.

Tiedtke, M.: A comprehensive mass flux scheme for cumulus parametrization in large-scale models, Mon. Weather Rev., 117, 1779–1800, 1989.

Tiedtke, M.: Representation of Clouds in Large-Scale Models, Mon. Wea. Rev., 121, 3040–3061, https://doi.org/10.1175/1520-0493(1993)121<3040:ROCILS>2.0.CO;2, 1993.

Tiedtke, M.: An extension of cloud-radiation parameterization in the ECMWF model: The representation of subgrid-scale variations of optical depth, Mon. Wea. Rev., 124, 745–750, 1996.

Tompkins, A.: Ice supersaturation in the ECMWF integrated forecast system, Q. J. Roy. Meteor. Soc., 133, 53–63, 2007

Tripoli, G. J., and W. R. Cotton: A numerical investigation of several factors contributing to the observed variable intensity of deep convection over south Florida, J. Appl. Meteor., 19, 1037–1063, 1980.

Williams, P.D.: A proposed modification to the Robert–Asselin time filter, Mon. Weather Rev. 137: 2538–2546, 2009.

1051   Weisman, M. L., Davis, C., Wang, W., Manning, K. W. and Klemp, J. B.: Experiences

1052   with 0–36-h explicit convective forecasts with the WRF-ARW model, Wea. Forecasting,

1053   23, 407–437, https://doi.org/10.1175/2007WAF2007005.1, 2008.

1054

1055   Weusthoff, T., Ament, F., Arpagaus, M. and Rotach, M. W.: Assessing the benefits of

1056   convection-permitting models by neighborhood verification: Examples from MAP D-

1057   PHASE, Mon. Wea. Rev., 138, 3418–3433, https://doi.org/10.1175/2010MWR3380.1,

1058   2010.

1059

1060   Zeng, X., Zhao, M. and Dickinson, R.E.: Intercomparison of bulk aerodynamic algorithms

1061   for the computation of sea surface fluxes using TOGA COARE and TAO data, J Clim 11:

1062   2628–2644, 1998.

1063

1064   Zhu, Y., and Newell, R. E.: A proposed algorithm for moisture fluxes from atmospheric

1065   rivers, Mon. Wea. Rev., 126, 725–735, https://doi.org/10.1175/1520-

1066   0493(1998)126<0725:APAFMF>2.0.CO;2, 1998